^{40}Ar–^{39}Ar dating of volcanogenic products from the AND-2A core (ANDRILL Southern McMurdo Sound Project, Antarctica): correlations with the Erebus Volcanic Province and implications for the age model of the core

Gianfranco Di Vincenzo[1]* · Laura Bracciali[2] · Paola Del Carlo[3] · Kurt Panter[4] · Sergio Rocchi[2]

[1]Istituto di Geoscienze e Georisorse, CNR, via Moruzzi 1, I–56124 Pisa, Italy

[2]Dipartimento di Scienze della Terra, Università di Pisa, Via S. Maria 53, I–56126 Pisa, Italy

[3]Istituto Nazionale di Geofisica e Vulcanologia, Sezione di Pisa, via della Faggiola 32, I-56126 Pisa, Italy

[4]Department of Geology, Bowling Green State University, Bowling Green, OH, 43403, USA

[accepted for publication in Bulletin of Volcanology]

*Corresponding author. Fax: +39 050 3125 360.

E-mail address: g.divincenzo@igg.cnr.it

Abstract The AND-2A drillcore (Antarctic Drilling Program – ANDRILL) was successfully completed in late 2007 on the Antarctic continental margin (southern McMurdo Sound, Ross Sea) with the aim of tracking ice-proximal to shallow marine environmental fluctuations and to document the 20-Ma evolution of the Erebus Volcanic Province. Lava clasts and tephra layers from the AND-2A drillcore were investigated from a petrographic and stratigraphic point of view and analyzed by the ^{40}Ar–^{39}Ar laser technique in order to constrain the age model of the core and to gain information on the style and nature of sediment deposition in the Victoria Land Basin since Early Miocene. Ten out of 17 samples yielded statistically robust ^{40}Ar–^{39}Ar ages, indicating that the AND-2A drillcore recovered ≤230 m of Middle Miocene (~128–358 meters below sea floor, ~11.5–16.0 Ma) and >780 m of Early Miocene (~358–1093 meters below sea floor, ~16.0–20.1 Ma). Results also highlight a nearly continuous stratigraphic record from at least 358 meters below sea floor down hole, characterized by a mean sedimentation rate of ~19 cm/ka, possible oscillations of no more than a few hundreds of ka and a break within ~17.5–18.1 Ma. Comparison with available data from volcanic deposits on land, suggests that volcanic rocks within the AND-2A core were supplied from the south, possibly with source areas closer to the drill site for the upper core levels, and from 358 meters below sea floor down hole, with the "proto-Mount Morning" as the main source.

Key words ANDRILL SMS · ^{40}Ar–^{39}Ar geochronology · Erebus Volcanic Province · McMurdo Sound · lava clasts · sedimentation rate · tephra layers · Victoria Land Basin

Introduction

In December 2007 the Antarctic Drilling (ANDRILL) program completed its second hole (AND-2A, Fig. 1) recovering 98% of the sediments cored to a depth of 1138.54 meters below the sea floor (mbsf) in McMurdo Sound (Florindo et al. 2008; Harwood et al. 2008). The fundamental goal of the ANDRILL program is to obtain from high-resolution sediment cores important new information about the Neogene Antarctic climate and evolution of Antarctic rift basins (http://andrill.org/). A focus of the Southern McMurdo Sound (SMS) project is to recover strata from the Middle Miocene, a period characterized by warmer conditions (Middle Miocene Climatic Optimum) followed by long-term climate change towards cold-polar conditions (Flower and Kennett 1994; Zachos et al. 2001; Holbourn et al. 2007; Zachos et al. 2008). This objective was accomplished, providing an expanded Early to Middle Miocene record (Harwood et al. 2008) and filling the gap left by previous drilling of older sediments (~34–17 Ma) recovered in the Cape Roberts project (CRP in Fig. 1 – Barrett 2007) and younger sediments (~14–0 Ma) recovered in the first ANDRILL hole (AND-1B, MIS in Fig. 1) during the McMurdo Ice Shelf project (Naish et al. 2007).

All the objectives of the SMS project rely heavily on the achievement of an age model for the core that is as accurate as possible. This study reports the entire set of ^{40}Ar–^{39}Ar data available from volcanogenic products of the AND-2A core in conjunction with petro-chemical and lithological data of the dated materials, with a twofold purpose. First to examine possible correlations with the activity of the Erebus Volcanic Province in order to constrain possible volcanic sources, and second to discuss the implications for the age model of the core and, more in general, for sedimentation in the Victoria Land Basin since Early Miocene.

Background

The AND-2A core

The AND-2A core contains terrigenous clastic lithologies ranging from claystones through siltstones and sandstones to conglomerates, breccias and diamictites. The core is subdivided into fourteen lithostratigraphic units on the basis of major changes in lithology with particular emphasis on diamictite abundance and associated sediments relative to other lithologies (Fielding et al. 2008b). Fielding et al. (2008b) identified thirteen recurring lithofacies interpreted to represent a wide spectrum of depositional environments ranging from minimally ice-influenced, shallow marine settings (e.g., diatomite and fossil-rich mudstone), through ice contact proglacial and glacimarine (e.g., ripple cross-laminated sandstone, interlaminated sandstone, siltstone and diamictite) to possibly subglacial environments (e.g., massive diamictite that shows extensive shear and rotation fabrics). The

lithologies are arranged vertically in a repetitive fashion through the length of the core and are divided into seventy sequences, each of which fine upward and are truncated by the next sequence boundary (Fielding et al. 2008b). Each sequence possibly represents a cycle of maximum ice advance followed by a transgression towards minimum ice conditions (C. Fielding, personal communication, 2009).

Volcanic material is persistent throughout the AND-2A core and is the dominant clast type (> 50%) in nine of the fourteen lithostratigraphic units (Panter et al. 2008). Lithostratigraphic Unit 1 corresponds to the top 37 meters of the core and is composed entirely of volcaniclastic sediments, including nearly primary tephra layers, clast-supported lava breccia and ripple cross-laminated vitroclastic sands. This unit is interpreted to represent shallow marine to emergent volcanism from a previously unknown volcano close to the drill site (Del Carlo et al. 2009). Volcanic material within the other thirteen lithostratigraphic units consist mostly of lava clasts found in coarse grained deposits (e.g., conglomerate, diamictite) and rare, primary to moderately reworked, tephra layers that occur as thin accumulations within sandstones and siltstones in the lower half of the hole (Panter et al. 2008).

Volcanism in the McMurdo Sound area

McMurdo Sound and the land surrounding it is an area with a rich history of rift-related alkaline volcanism. Large volcanoes include Mount Erebus (~2000 km^3), Mount Terror and Mount Bird, which form Ross Island, and Mount Discovery, Minna Bluff and Mount Morning located on the mainland (Fig. 1). These volcanoes as well as many smaller volcanic centers (e.g, Brown Peninsula, White and Black Islands) and volcanic fields (foothills of Royal Society Range, Wright-Taylor Valleys, Dailey Islands group) are part of the Erebus Volcanic Province of the McMurdo Volcanic Group (Kyle and Cole 1974; Kyle 1990a, 1990b). The Erebus Volcanic Province represents the largest area of exposed Late Cenozoic volcanic rocks and the longest and most complete record of alkaline volcanism in Antarctica. The volcanic deposits on land range in age from approximately 19 Ma to current Strombolian-style activity within the summit crater of the Erebus Volcano (Dibble et al. 2008: Kelly et al. 2008). Evidence for older activity is from volcanoclastic sediments and tephra found in drill cores (CIROS-1, MSSTS-1, Cape Roberts and AND-2A) and extends the history of alkaline volcanism in this area back to 26–20 Ma (Gamble et al. 1986; Barrett 1987; McIntosh 1998, 2000).

The volcanism is located in the southern portion of the Victoria Land Basin, one of four major rift-related basins within the Ross Sea (Fig. 1b), which along with the Transantarctic Mountains, are components of the West Antarctic rift system (Van der Wateren and Cloetingh 1999). Extension, rifting and basin subsidence began in the Eocene to Early Oligocene (Fielding et al. 2008a). On the basis of drillhole and seismic reflection studies (Fielding et al. 2008a and references therein) the Victoria Land Basin evolved in a series of

intervals each reflecting changes in basin forming tectonic processes. A phase of renewed rifting during the Middle to Late Miocene in the southern Victoria Land Basin produced the Terror Rift (Wilson 1995, 1999; Fielding et al. 2008a). Volcanism in the Erebus Volcanic Province exploited structural weaknesses associated with the Terror Rift and Discovery Accommodation Zone (Fig. 1b), a transverse boundary that segments the rift (Cooper et al. 1987; Wilson 1999; Johnston et al. 2008). Volcanic vents appear to be aligned along major normal faults and transverse lineaments with large volcanoes located at the intersection of these structures (Wilson 1999). There also appears to have been a broad shift in the main centers of volcanism from the continent, well within the accommodation zone (base of Mount Morning, Mason Spur), to the northeast into the center of the rift (i.e. Ross Island and Franklin Islands) beginning around 13 Ma. One interpretation of the structure/volcanic relationship is that a regional transtensional neotectonic regime controls the volcanic patterns and has formed stress-controlled linear fissure arrays and reactivated pre-existing structures (Wilson 1999; Wilson and Demosthenous 2000; Wilson et al. 2003; Johnston et al. 2008). An alternative explanation involving mantle plumes has also been proposed to explain the high volumes of evolved erupted material and the three-armed pattern of volcanism centered around Mount Erebus on Ross Island and Mount Discovery on the continent (Kyle 1990b; Kyle et al. 1992). The age and compositional data from volcanic materials recovered in the AND-2A core will be used to constrain the evolution of the Erebus Volcanic Province and, by virtue of their intimate association with the tectonic, sediment and climate records, the factors that controlled its development.

The geochemistry of lava clasts and glass separated from tephra and volcaniclastic sediments indicate that all of the volcanic material in the AND-2A core is of alkaline affinity and the majority plots within the known compositional field of the Erebus Volcanic Province (Panter et al. 2008; Del Carlo et al. 2009). Lava clasts and glass from the core are compositionally diverse and include variably alkaline compositions (e.g., the *ne*-normative content of the lava clasts ranges from 0 to 16) that represent both moderately silica-undersaturated and highly silica-undersaturated alkaline magma lineages. In terms of evolutionary degree, both affinity lineages include primitive to weakly evolved samples (alkali basalt and basanite, respectively) along with strongly evolved ones (trachyte and phonolite, respectively). It is noteworthy that the most evolved samples (trachyte and rhyolite) from the moderately alkaline lineage have a peralkaline chemical signature that is only found at Mount Morning (Kyle 1990a). Finally, the whole rock clasts and glass shard compositions from AND-2A core display a very limited overlap with the volcanic glasses from the McMurdo Ice Shelf project (MIS, Fig. 1) AND-1B core (Pompilio et al. 2007). This distinction might indicate an important spatial and temporal change in the chemical evolution of the volcanic activity in the region.

^{40}Ar–^{39}Ar data: results and interpretation

In this section we report and interpret ^{40}Ar–^{39}Ar data for a sub-set of 17 samples, consisting of clasts and primary to moderately reworked tephra layers. These samples were selected after careful examination of 33 specimens, initially selected for dating on the basis of on-ice descriptions (Fielding et al. 2008b; Panter et al. 2008). Nine out of the 14 identified lithostratigraphic units (i.e., 1, 4, 7, 8, 9, 10, 11, 12, and 14) contained suitable materials for dating, consisting of volcanic lava clasts or pumice-rich layers. In contrast, within the remaining 5 lithostratigraphic units (i.e., 2, 3, 5, 6 and 13) datable volcanogenic products were not found. The main features of selected samples along with the degree of reworking are summarized in Table 1. More details on the petrographic features, along with the analytical procedures and full ^{40}Ar–^{39}Ar data, are given in the Electronic Supplementary Material (ESM). Ages were calculated using the IUGS recommended constants (Steiger and Jäger 1977), in order to allow direct comparison with previously published Ar data. However, in discussion section, we examine the effects in the calculated ages of the recently recognized problems in the ^{40}K decay constants (e.g., Min et al. 2000; Schoene et al. 2006) and of the possible solution proposed by Kuiper et al. (2008).

Lithostratigraphic Unit 1 (0 – 37.01 mbsf)

Phonolite clast 8.88–9.02 mbsf represents the uppermost sample analyzed of the whole set (Table 1). The large-sized alkali feldspar crystals (up to a few centimetres) were crushed and sieved to the 300–500 μm grain size in order to facilitate the removal of melt inclusions during the leaching procedure. After leaching however, several grains still preserved numerous internal melt inclusions. Sample was first analyzed by the ^{40}Ar–^{39}Ar total fusion technique applied to mg-sized splits (see Table S1 in the ESM). Four total fusion analyses gave apparent ages overlapping within analytical errors, with an error-weighted mean age of 0.124±0.014 Ma (±2σ internal error), a Mean Square of Weighted Deviates (MSWD) of 0.59 and a constant K/Ca ratio (Fig. 2). In an ^{36}Ar/^{40}Ar vs. $^{39}Ar_K$/^{40}Ar isochron plot (not shown), data are poorly scattered and define a slightly younger intercept age of 0.107±0.039 Ma (±2σ internal error, MSWD = 0.89) and an initial ^{40}Ar/^{36}Ar ratio of 301±11, within error with that of modern atmospheric Ar (^{40}Ar/^{36}Ar = 295.5). A step-heating run on the same mineral concentrate was performed in order to verify the behaviour of the sample when subjected to incremental heating. Alkali feldspar 8.88–9.02 mbsf yielded a discordant hump-shaped age profile (Fig. 3), with apparent ages ranging from 0.053±0.022 to 0.220±0.026 Ma (±2σ analytical errors), attesting to sample heterogeneity not revealed by total fusion analysis. The total gas apparent age from step-heating data is 0.127±0.012 Ma (±2σ analytical error), and closely matches those from total fusion data. An $^{40}Ar^*/^{39}Ar_K$ vs. $^{38}Ar_{Cl}/^{39}Ar_K$ three-isotope correlation diagram

(converted to age and Cl/K ratio – Fig. 4) of data from both total fusion and step-heating analyses reveals a fairly well-defined positive correlation for the whole data set, suggesting that the system is dominated by binary mixing between two end-members: (1) a high $^{40}Ar^*/^{39}Ar_K$ and Cl/K component and (2) a component with a lower $^{40}Ar^*/^{39}Ar_K$ ratio and a Cl/K ratio close to zero. A similar positive correlation has been documented for alkali feldspar phenocrysts from Mount Erebus and assigned to trapped excess argon (i.e., parentless ^{40}Ar) hosted in melt inclusions along with Cl within the alkali feldspar (Esser et al. 1997). Taking into account that the alkali feldspar does not accommodate Cl in its crystal lattice, and assuming that the system consists of a simple binary mixture (i.e., alkali feldspar with no excess Ar and Cl and melt inclusions with both excess Ar and Cl), then the true Ar age should be defined in Fig. 4 by the extrapolation of the trend to the *y*-axis at a Cl/K ratio of zero. A least-squares fit for the whole data set yields a *y*-intercept age of 0.035±0.045 Ma and a MSWD of 2.0 (Fig. 4), attesting to a slight excess of scatter exceeding analytical uncertainties (probability of fit 0.021). Excluding step no. 3 (Fig. 4), we obtain a comparable but more precise intercept age of 0.057±0.023 Ma and a statistically acceptable MSWD of 0.93 (probability of fit 0.51). In light of the above arguments, we conservatively interpret Ar data from alkali feldspar 8.88–9.02 to indicate an eruption age ≤0.080 Ma for the phonolite.

The groundmass of the basanite lava clast from the 10.22–10.44 mbsf interval, yielded an internally discordant age spectrum with a descending shape and a total gas apparent age of 0.662±0.042 Ma (±2σ interal error). Similar age spectra are common for volcanic groundmass and are explained by loss and/or redistribution of neutron-produced $^{39}Ar_K$ and $^{37}Ar_{Ca}$ during sample irradiation (e.g., Koppers et al. 2000). Four consecutive steps from the intermediate-temperature region, representing ~60% of the total $^{39}Ar_K$ released, define a concordant segment (MSWD = 0.59) yielding an error-weighted mean age of 0.692±0.038 Ma (±2σ internal error). This age matches the intercept age of ~0.691 Ma derived from isochron analysis of the four steps in a $^{36}Ar/^{40}Ar$ vs. $^{39}Ar_K/^{40}Ar$ plot (initial $^{40}Ar/^{36}Ar$ ratio of 295.7±5.5). The weighted mean age of 0.692±0.038 Ma overlaps within analytical errors with the total gas age and is taken as the eruption age of the basanitic lava.

The hawaiite clast from the 12.23–12.41-mbsf interval yielded a comparable shaped age profile as the previous sample, though a significant concordant segment is not defined (Fig. 3). However, two consecutive steps (representing ~33% of the total $^{39}Ar_K$ released), characterized by the highest radiogenic Ar contents and comparable Ca/K ratios (no. 3 and 4, Table S1 in the ESM), overlap within errors and yield a weighted mean age of 0.793±0.063 Ma (±2σ internal error), in close agreement with the total gas age (0.758±0.090 Ma). The 0.793±0.063-Ma is taken as the best age constraint derivable for clast 12.23–12.41 mbsf.

Two other mafic lava clasts were examined from the Lithostratigraphic Unit 1 but yielded anomalously old preliminary total fusion ages of 16.1±2.2 and 9.5±1.2 Ma (sample 18.03–18.25 and 18.69–18.73 mbsf, respectively; Table S1 in the ESM), that although affected by large uncertainties, suggest that clasts were transported and reworked long before they were

deposited at the level of sampling. Given the much older age than those reasonably expected for sediments at 18–19 mbsf, step-heating experiments on these two samples were not completed.

Lithostratigraphic Unit 4 (122.86 – 224.82 mbsf)

A felsic lava clast from the 127.50–127.52 mbsf interval was analyzed by the ^{40}Ar–^{39}Ar total fusion technique on single to a few alkali feldspar grains. The whole set of data (12 analyses, Table S1 in the ESM) gives in a cumulative probability plot (Fig. 2) a nearly single-mode distribution, typical of within-sample homogeneity of data. The error-weighted mean of the twelve total fusion analyses is 11.369±0.074 Ma (±2σ internal error), MSWD 1.6 and probability of fit only 0.078. Analyses no. 9, along with 7 and 8 (Table S1 in the ESM), were obtained from a single millimetre-sized alkali feldspar phenocryst, which may be potentially affected by the presence of inherited Ar due to a protracted crystallization history, as demonstrated for volcanic rocks from other areas (e.g., Bachmann et al. 2007). Omitting analysis no. 9, which gave the most (oldest) discordant age, then the error-weighted mean is 11.363±0.072 Ma (±2σ internal error), the MSWD 1.00 and the probability of fit 0.44. This age is taken as the best age estimate for the felsic lava.

In the slightly deeper 129.96–129.97 mbsf interval of Lithostratigraphic Unit 4, a plagioclase separate from a basaltic clast was analyzed by the step-heating technique. A split of a few tens of milligrams of plagioclase separate was incrementally heated until fusion over eight steps and yielded an internally concordant age profile (Fig. 3). The first three steps are characterized by a low to very low radiogenic Ar contents (down to 0.1 %) and, consequently, are affected by large analytical errors. However steps 4 to 8 display much lower atmospheric Ar contents ($^{40}Ar^*$ contents up to ~60%, Table S1 in the ESM) and yield smaller analytical errors. The error-weighted mean age calculated using all steps is 11.43±0.46 Ma (±2σ internal error, MSWD = 0.71), within error with the isochron age of 11.39±0.49 (initial $^{40}Ar/^{36}Ar$ ratio of 296.0±2.3) and is therefore statistically indistinguishable from the age of clast 127.50–127.52.

Lithostratigraphic Unit 7 (339.92 – 436.18 mbsf)

In the Lithostratigraphic Unit 7 only an intermediate lava clast, collected from the 358.11–358.13-mbsf interval, was investigated and analyzed by the laser step-heating extraction technique on a few tens of milligrams of groundmass separate. The age spectrum compares in shape with those of groundmasses from the Lithostratigraphic Unit 1 (Fig. 3), yet data are much more precise due to the comparatively much higher radiogenic Ar contents (Table S1 in

293 the ESM). Four consecutive steps from the intermediate temperature region, characterized by
294 the highest radiogenic Ar contents, similar K/Ca ratios, and representing together ~50 % of
295 the total $^{39}Ar_K$ released, define a concordant segment (MSWD = 2.2, probability of fit 0.083)
296 yielding an error-weighted mean age of 15.91±0.14 Ma. This date overlaps within error limits
297 with the less precise intercept age of 15.74±0.29 Ma (±2σ analytical error) from isochron
298 analysis and is considered a reliable eruption age.
299
300
301 Lithostratigraphic Unit 8 (436.18 – 608.35)
302
303 The intermediate lava clast from the 440.83–440.86-mbsf interval gave a poor alkali feldspar
304 crystal yield, which, under a stereomicroscope, appeared to be contaminated by rounded
305 quartz and plagioclase. Total fusion analyses were attempted on single feldspar grains and
306 yielded a wide range of ages, from 16.23±0.77 to ~700 Ma thus attesting to contamination of
307 the mineral concentrate by grains derived from the crystalline basement. The two youngest
308 total fusion analyses match within errors, and gave an error-weighted mean age of 16.54±0.34
309 Ma. This age, yet quite imprecise, represents a maximum age estimate for the time of
310 deposition at the 440.83–440.86-mbsf interval.
311 Mineral separation from a felsic lava clast of the same lithostratigraphic unit, from the
312 564.92–564.93-mbsf interval, gave euhedral alkali feldspar, some of which sufficiently large to
313 be analyzed by single-grain total fusion analysis. Seven out of sixteen runs were completed
314 on single grains and the remaining on a few grains (3 to 5, Table S1 in the ESM). The whole
315 set of data, when plotted in a cumulative probability distribution diagram, exhibits a well-
316 defined single-mode distribution attesting to homogeneity of data. The error-weighted mean
317 age for the sixteen analyses is 17.10 ±0.14 Ma and is taken as the age of the felsic lava.
318
319
320 Lithostratigraphic Unit 9 (607.35 – 648.74 mbsf)
321
322 From Lithostratigraphic Unit 9 down hole, studied samples consist of primary to moderately
323 reworked tephra-rich layer thus providing the most robust age determinations for the whole
324 AND-2A core. ^{40}Ar–^{39}Ar age data were performed using the total fusion technique, whenever
325 possible, on single crystals. When crystals were too small to yield reasonably precise age
326 determinations, total fusion analyses were performed on multi-grain splits. Numbers of
327 crystals used in each run are listed in Table S1 of the ESM.
328 Mineral separation on the 640.13–640.16 tephra layer gave mostly euhedral to subhedral
329 alkali feldspar grains which however were not large enough for single-grain analyses. Total
330 fusion experiments were therefore chiefly performed on splits consisting of a few crystals
331 that, in a cumulative probability distribution plot (Fig. 2), yield a single-mode distribution

and an error-weighted mean age of 17.39±0.11 Ma (±2σ internal error, MSWD = 1.4 and probability of fit 0.14). A least squares fit in a $^{36}Ar/^{40}Ar$ vs. $^{39}Ar_K/^{40}Ar$ isochron diagram (Fig. 5) through the seventeen data points yields a nominally younger age of 17.302±0.069 Ma (±2σ analytical error) and an initial $^{40}Ar/^{36}Ar$ ratio of 360±39, significantly higher than that of modern atmospheric Ar. This in principle indicates that alkali feldspar 640.13–640.16 may be slightly contaminated by excess Ar thereby suggesting that the best age estimate for the tephra should be that derived from isochron analysis. However, close inspection of Fig. 5 reveals that the slope of the regression line is strongly dependent on one data point (analysis no. 11), which is characterized by the lowest radiogenic Ar content (Table S1 in the ESM). Excluding this analysis from the regression calculation then the *y*-intercept becomes indistinguishable at the 2σ confidence level (362±76) from that of modern atmospheric Ar and the *x*-intercept age 17.300±0.099 Ma (±2σ analytical error), is well within 1σ error with the error-weighted mean age. The latter is taken as the age of alkali feldspar, and given the primary character of the tephra layer, the 17.39±0.11-Ma age represents a meaningful estimate for depositional age of the 640.13–640.16-mbsf interval.

Lithostratigraphic Unit 10 (648.74 – 778.34 mbsf)

The two pumice layers from the 709.14 to 709.19 mbsf interval (samples, 709.14–709.16 and 709.17–709.19) yielded alkali feldspar crystals insufficiently large (<<1 mm in length) for single-grain total fusion analyses. Furthermore mineral concentrate from both samples contained anhedral plagioclase and rounded quartz grains that, in agreement with petrographic results (see ESM), indicate the presence of an older detrital component. Multi-grain splits from sample 709.14–709.16 yielded a wide range of age from ~18.1 to ~240 Ma (Fig. 2 and Table S1 in the ESM). However, six out of ten analyses yielded the youngest ages and a statistically acceptable error-weighted mean of 18.15±0.18 Ma (±2σ internal error, MSWD = 0.95, probability of fit 0.45). Similarly, sample 709.17–709.19 gave a wide range of apparent ages (Fig. 2 and Table S1 in the ESM). Younger ages are in line with the mean age of sample 709.14–709.16, but the remaining data yield older apparent ages (up to ~100 Ma) associated to higher Ca/K ratios (Table S1 in the ESM) and indicating contamination by older detrital plagioclase. The younger five out of ten analyses gave an error-weighted mean age of 17.93±0.28 Ma (MSWD = 0.83) that is indistinguishable at the 1σ confidence level from the mean age of sample 709.14–709.16 mbsf. The ~18-Ma age is therefore taken as a close approximation of the time of deposition of sediments at 709.14 to 709.19 mbsf interval.

Lithostratigraphic Unit 11 (778.34 – 904.66 mbsf)

The pumice concentration from the 831.66–831.68-mbsf interval yielded a crystal separate characterized by mostly millimetre-sized euhedral grains. Eleven out of fifteen ^{40}Ar–^{39}Ar runs were completed on single grains and the remaining analyses on splits consisting of three grains. The whole data set defines in a cumulative probability plot a single-mode distribution and an error-weighted mean age of 18.71±0.12 (±2σ internal error, MSWD = 0.93, probability of 0.53), well distinguishable at the 2σ confidence level from the mean age of the previous sample. Given the nearly primary character of this tephra layer, the mean age of alkali feldspar is taken as the depositional age of the 831.66–831.68-mbsf interval.

Lithostratigraphic Unit 12 (904.66 – 996.69 mbsf)

Alkali feldspar separates from both samples (953.28–953.31 and 953.54–953.56) of the 953.28–953.56-mbsf interval, consist of euhedral grains, which were mainly analyzed by total fusion analyses on single crystals and gave intrasample concordant ages within analytical errors (Fig. 2). Error-weighted mean ages are 19.44±0.12 Ma (±2σ internal error, MSWD = 1.06, probability 0.39) and 19.49±0.14 Ma (±2σ internal error, MSWD = 1.11, probability 0.35) for sample 953.28–953.31 and 953.54–953.56, respectively, and are therefore indistinguishable at the 1σ confidence level. These ages represent a reliable estimate for the depositional age of the 953.28–953.56-mbsf interval.

Lithostratigraphic Unit 14 (1040.28 – 1138.54)

Tephra layer 1093.00–1093.04 represents the deepest sample investigated and comes from less than 50 m from the bottom of the AND-2A core (1138.54 mbsf). The mineral concentrate consisted of euhedral millimetre-sized alkali feldspar grains. Eighteen single-grain total fusion analyses yielded an error-weighted mean with a probability of fit $<<0.05$, attesting to an excess of scatter exceeding analytical uncertainties and indicating intrasample heterogeneity (Fig. 2 and Table S1 in the ESM). However, the excess of scatter is due to only one analysis (no. 9, Table S1 in the ESM). If this run is taken as an outlier and is omitted from the weighted mean calculation, then the probability of fit is 0.32, with an error-weighted mean age of 20.01±0.12 Ma. This age is again statistically distinguishable from those of the previous samples and is considered a reliable estimate of depositional age at the 1093.00–1093.04-mbsf interval.

Discussion

410 Influence of the "inaccuracy" of ^{40}K decay constants
411
412 ^{40}Ar–^{39}Ar geochronological data presented above, have yielded 10 statistically robust age
413 determinations, 5 of which directly constraining the time of deposition at the level of
414 sampling. Possible volcanic sources and the implications for the age model of the core and,
415 more generally, for the time, rate and nature of sediment deposition in the Victoria Land
416 Basin since Early Miocene, are discussed in the specific sections below. Age data obtained in
417 the present study are summarized in Table 2 and have been calculated using both the IUGS
418 recommended ^{40}K decay constants (Steiger and Jäger 1977), along with an age of 28.03 Ma for
419 the FCs standard (Jourdan and Renne 2007), and the more realistic constants recently
420 proposed by Kuiper et al. (2008).
421 It is important to recall here that the ^{40}Ar–^{39}Ar method is inherently a relative technique
422 in that ages are calibrated against those of neutron-fluence monitors (dating standards) and
423 calculated using available ^{40}K decay constants. This implies that the accuracy of a ^{40}Ar–^{39}Ar
424 age is limited by the accuracy of primary standards as well as by the precision and accuracy
425 of intercalibrations among standards and of the ^{40}K decay constants (e.g., Renne et al. 1998).
426 This is a critical issue because whenever Ar ages are used in "absolute" sense or are
427 compared to age data derived from other radioisotopic or non-radioisotopic techniques, the
428 uncertainty in age should include all known sources of error, including those associated to
429 the calibration of the fluence monitor and of ^{40}K decay constants. If on the one hand the
430 uncertainty on the calibration of the FCs dating standard against primary standards (age
431 based on $^{40}Ar^*$ determined by "first principle") has been recently and significantly improved
432 (Jourdan and Renne 2007), on the other hand, the ^{40}K decay constants are currently under
433 scrutiny, particularly the ^{40}K branching ratio. At present, most of the uncertainty associated to
434 a ^{40}Ar–^{39}Ar age, when all sources of systematic errors are considered, is indeed due to
435 uncertainties in radioactive decay rates (e.g., Renne et al. 1998). The basis for the ^{40}K decay
436 constants in current use by geochronologists was discussed in detail by Min et al. (2000), who
437 noted that the ^{40}K decay constants used in geochronology since 1977 (Steiger and Jäger 1977)
438 are quite different from those used by the nuclear physics community and concluded that the
439 total ^{40}K decay constant is known to no better than ±2% (2σ level). The detrimental effect of
440 the uncertainties in ^{40}K decay constants on a ^{40}Ar–^{39}Ar age is evident from Table 2: internal
441 errors as low as 0.6–0.7% (e.g., samples 127.50–127.52 or 1093.00–1093.04) become as large as
442 1.7–1.8% when individual errors also include uncertainties in the ^{40}K decay constants.
443 The lack of accuracy in the currently used ^{40}K decay constants is confirmed by the
444 growing body of data from rapidly cooled rocks indicating that ^{40}Ar–^{39}Ar ages tend to be
445 systematically ≤1% younger than U–Pb ages (e.g., Min et al. 2000; Krumrei et al. 2006;
446 Schoene et al. 2006). Since U decay constants are the most accurately known, reconciliation of
447 ^{40}Ar–^{39}Ar and U–Pb ages requires that either the age of the ^{40}Ar–^{39}Ar standard is older, or the
448 total ^{40}K decay constant is smaller (Min et al. 2000). A possible solution to this problem has

been recently proposed by Kuiper et al. (2008), who, comparing astronomical and ^{40}Ar–^{39}Ar ages of tephra in marine deposits and, assuming a more realistic total ^{40}K decay constant of (5.463±0.214) $\cdot 10^{-10}$ a^{-1} (Min et al. 2000), obtained an age for FCs of 28.201±0.046 Ma (±2σ, incorporating all sources of error), that is 0.65% older and over 6 times more precise than the most recently calibrated age against primary standards (Jourdan and Renne 2007). More significantly, the age of the standard proposed by Kuiper et al. (2008) was evaluated independently from the ^{40}K decay constants, with the implication that the calculation of the age for an unknown sample calibrated against the FCs monitor only involves the ^{40}K total decay constant, and consequently it is nearly insensitive to the value adopted and to its uncertainty (Kuiper et al. 2008). As an example (see Table 2), using a total ^{40}K decay constant of (5.463±0.214) $\cdot 10^{-10}$ a^{-1} (Min et al. 2000) and an age of 28.201±0.046 Ma (Kuiper et al. 2008) for FCs, we obtain for sample 127.50–127.52 an error-weighted mean age of 11.432±0.091 Ma, which becomes 11.433±0.091 Ma when the calculation assumes a total ^{40}K decay constant of 5.543±0.020 $\cdot 10^{-10}$ a^{-1} (Steiger and Jäger 1977).

Correlation with the Erebus Volcanic Province and possible volcanic sources

The geochronological data based on available K–Ar and ^{40}Ar–^{39}Ar analyses on whole rocks, groundmasses or mineral separates from volcanic rock samples of the Erebus Volcanic Province are summarized in Fig. 6 (a, b, c, d) and compared with ^{40}Ar–^{39}Ar ages from this work and from previous drill cores (Fig. 6e). Age data quoted in this section and shown in Fig. 6, were all calculated using the IUGS recommended ^{40}K decay constants (Steiger and Jäger 1977) in order to be consistent with previously published Ar data. Errors on ^{40}Ar–^{39}Ar ages are given as 2σ internal uncertainties and ages are consistent with the up-to-date age of the FCs monitor (see caption of Fig. 6). Errors on K–Ar ages are those originally reported by the authors.

Figure 6 shows that the volcanic activity in the area was nearly continuous since Early Miocene and progressively propagated toward northeast, with ages of volcanic deposits on land ranging from ~19 Ma (oldest K–Ar whole rock age from Mount Morning) to Recent (Mount Erebus). Furthermore, previous drill cores in the Cape Roberts area (CRP-1 and CRP-2A; Barrett 2007 – Fig. 1) extend the volcanic activity in the area back to the Late Oligocene (McIntosh 1998, 2000).

Sample 8.88–9.02 from the Lithostratigraphic Unit 1, with its young eruption age of <80 ka (Table 2), phonolite composition and large alkali feldspar phenocrysts rich in melt inclusions, compares remarkably with volcanic products from Mount Erebus (Kyle et al. 1992; Esser et al. 2004; Kelly et al. 2008). However as discussed in Del Carlo et al. (2009), this sample most probably represents a glacial dropstone and it is not truly part of the Lithostratigraphic Unit 1. Clasts 10.22–10.44 and 12.23–12.41 have basaltic compositions and compositionally

and temporally match the products of the volcanic activity documented for Dailey Islands (~15 km to the south-southwest of the SMS drill site, Fig. 1). These samples are interpreted to be sourced from local vents associated with a submerged extension of the Dailey Islands volcanic field (Del Carlo et al. 2009). The basaltic samples 18.03–18.25 and 18.69–18.73, both display ages (~16 and ~10 Ma, respectively) significantly older than those reasonably assumed for the depth of sampling (Fig. 7). These samples therefore were long reworked before final deposition and the older basalt may represent materials transported by the Koettliz Glacier to the McMurdo Ice Shelf from deposits on the north side of Mount Morning (e.g., Kyle and Muncy 1989; Kyle 1990b). The composition (Del Carlo et al. 2009) and age of the younger sample (18.69–18.73) correlate well with volcanic deposits found along the eastern end of Minna Bluff (i.e., Minna Hook; Fig. 1).

Samples 127.50–127.52 and 129.96–129.97 from the Lithostratigraphic Unit 4 are clasts of different composition, felsic vs. basaltic, that yielded indistinguishable ages falling at the Middle/Late Miocene boundary (~11.4 Ma, Table 2). Possible sources for these samples (Fig. 6) are volcanic rocks from Mason Spur (Kyle 1990b) and/or Minna Bluff (Kyle 1990b; Fargo et al. 2008). Indeed, the age of volcanic products from both Minna Hook (11.86±0.06 to 11.20±0.10 Ma; Fargo et al. 2008) and Mason Spur (11.4±0.2, 11.7±0.4 and 12.1±0.2 Ma, Wright–Grassham 1987; 11.4±0.1 Ma, Martin et al. 2009) match those found for the investigated samples from the Lithostratigraphic Unit 4. However, the composition of volcanic rocks from Minna Bluff is overall more alkaline, plotting close to the trachyte-phonolite join, thus making provenance from Mason Spur more likely. If this is the case, ice flow or ocean currents were able to transport volcanic clasts from Mason Spur to the north without obstruction.

Samples from Lithostratigraphic Unit 7 to 14 (358.11–358.13 to 1093–1093.04) yielded ages in the range of 15.91±0.14 to 20.01±0.12 Ma (Table 2 and Fig. 6). Volcanic deposits on land with ages falling within this time interval are only known for the older deposits of Mount Morning, cropping out on its northern slopes above the Koettliz Glacier side (Gandalf Ridge; Fig. 1). K–Ar ages for rock samples from this area, varying in composition from trachyandesite to comenditic trachyte, are in the range of 15.5±0.5 to 18.73±0.32 Ma (Kyle and Muncy 1989). Comparable or even older ages (up to 25.69±0.16 Ma, Fig. 6) are known for groundmasses and alkali feldspar separates from ash layers or lava clasts sampled in the Cape Roberts drill cores (McIntosh 1998, 2000). The AND-2A core therefore contains the oldest known volcanogenic products of the Erebus Volcanic Province after those recovered from the Cape Roberts drill cores. On the basis of the data available so far, lava clasts in the AND-2A core sampled below ~350 mbsf and with ages older than ~15.5 Ma, were most likely derived from deposits on Mount Morning. Furthermore, explosive activity that produced the tephra found in AND-2A and Cape Roberts cores, as well as older (>13 Ma) tephra deposits in the Dry Valleys (Marchant et al. 1996; Lewis et al. 2007) were likely sourced from vents that have been eroded or are buried beneath the younger deposits on Mount Morning. A "proto-

Mount Morning" source for most if not all Early Miocene to Late Oligocene volcanism in the Erebus Volcanic Province is consistent with the progressive shift in volcanic activity away from the continent (i.e. the Mount Morning area) beginning around 13 Ma. Results from the present study reinforce the notion that the Mount Morning is a long-lived eruptive centre, a feature which has been explained by its position on the active West Antarctic Rift System, within the stationary Antarctic plate (Martin et al. 2009).

Implications for the age model of the AND–2A core and for sediment deposition in the Victoria Land Basin since the Early Miocene

Other age constraints (magnetostratigraphic and paleontological temporal constraints, and ages based on Sr isotope compositions of shell fragments), useful for the age model of the AND-2A core, are discussed in Acton et al. (2008a, b) and Taviani et al. (2008), and are compared to the whole set of ^{40}Ar–^{39}Ar data in Fig. 7. Note that the geological polarity time scale (GPTS) of Gradstein et al. (2004) for the last 23 Ma (Neogene), which was used in Acton et al. (2008a, b), is based on astronomical cycles in sediments (orbitally tuned with 40 ka accuracy) and is therefore independent of radioisotopic dating. ^{40}Ar–^{39}Ar ages quoted in this section and followed by subscript (K) refer to ages calculated using constants from Kuiper et al. (2008) and are considered to be more reliable than those calculated using ^{40}K decay constants in current use by geochronologists (see above).

In the 0–44.06-mbsf interval, encompassing the Lithostratigraphic Unit 1 and the first 7 m of Lithostratigraphic Unit 2, no age diagnostic taxa were observed (Taviani et al. 2008). In addition, due to the coarse grain size of lithologies encountered in the upper part of the core, interpretation of paleomagnetic data from the Lithostratigraphic Unit 1 to 4 (0–224.82 mbsf) was problematic (Acton et al. 2008a, b), with the only exception being the possible Brunhes/Matuyama reversal (0.781 Ma) or, and alternatively, any other reverse-to-normal transition younger than 2.5 Ma, encountered at 31.10 mbsf. This implies that the only direct temporal constraints for Lithostratigraphic Unit 1 come from ^{40}Ar–^{39}Ar data on volcanic clasts. As discussed above, petrographic and geochronological data allow the correlation of clast 8.88–9.02 to the pre-caldera summit flows of Mount Erebus. This would imply a sediment supply to the basin from the north and an unlikely very fast subsidence rate (>~500 cm/ka). However, most probably this sample is not truly part of the Lithostratigraphic Unit 1, being its position in the core simply coincidental and a product of recent glacial drift (Del Carlo et al. 2009). Among the remaining four mafic clasts, samples 18.03–18.25 and 18.69–18.73 gave unrealistically old ages for the depth of sampling, consistent with a long transport and reworking before final deposition, whereas samples 10.22–10.44 and 12.23–12.41 provide more realistic ages for the depth of sampling ($0.696\pm0.040_{(K)}$ and $0.798\pm0.065_{(K)}$ Ma, respectively; Table 2). These ages, although strictly constraining maximum ages of

deposition, suggest that the first 16 metres of the core are younger than 1 Ma. More significantly, in light of the 380 m water depth at the site of drilling and of evidence for shallow water sedimentation for the whole Lithostratigraphic Unit 1 (down to ~37 mbsf; Del Carlo et al. 2009), these data suggest that the mean rate of sedimentation (≤1.5±3.2 and 1.5±4.0 cm/ka, ≤2.0±1.4 cm/ka when both samples are used together) did not keep pace with that of basin subsidence (mean rate ≥56.1±3.2 and 49.2±4.0 cm/ka), the latter being ~40 times faster. Further, the alignment of Ar data in a depth vs. age diagram suggests that the reverse-to-normal transition encountered at 31.10 mbsf most probably corresponds to the boundary between Chron C2n and C2r.1r (1.945 Ma).

No age data have been obtained for Lithostratigraphic Unit 2 and 3 (37.07 to 122.86 mbsf) but two clasts from the Lithostratigraphic Unit 4 (127.50–127.52 and 129.96–127.97) yielded concordant ages of $11.432\pm0.091_{(K)}$ and $11.50\pm0.48_{(K)}$ Ma that overlap within internal errors (Table 2). These ages match a Sr isotope age of ~11.7 Ma from the 144.03–144.06 mbsf interval (Acton et al. 2008a) and are in line with the maximum age of deposition of 11.04 Ma for the 83.76–83.80-mbsf interval, inferred from foraminifera data (Taviani et al. 2008). Our geochronological data along with the independent age constraints suggest that sediments in the upper part of Lithostratigraphic Unit 4 were deposited at the Late/Middle Miocene boundary.

From the Lithostratigraphic Unit 6/7 boundary (339.92 mbsf) to the base of hole, samples investigated by the ^{40}Ar–^{39}Ar method are more uniformly distributed (Fig. 7). This, along with paleomagnetic data, whose quality below the Lithostratigraphic Unit 7/8 boundary improves significantly so as to provide a continuous polarity stratigraphy for the ~340–1139-mbsf interval (Acton et al. 2008a, b), allows the reconstruction of a robust age model and, more in general, a thorough comparison between temporal constraints based on radioisotopic and paleomagnetic data. Analyzed samples from the ~358–1093-mbsf interval consist of 3 clasts and 7 samples from primary to moderately reworked tephra layers, the former covering the uppermost part of the core interval (from ~358 to ~565 mbsf) and the latter the lowermost ~450 m (from ~640 to the base of the hole). In a depth vs. age plot (Fig. 7), data from the 3 clasts are aligned along the same trend with a negative slope defined by the seven tephra layers, suggesting that the 3 clasts yield Ar ages which closely approach the time of deposition and that the whole sample set provide a nearly continuous depositional record. A least-squares fit for the whole set of data using internal errors (Fig. 7a) yields a MSWD of 3.4 and a slope of 17.3±1.3 cm/ka. The MSWD value, although surprisingly low for a core ~735 metres in length, and corresponding to a time interval of ~4.1 Ma, given the degrees of freedom of the whole data set (i.e., 8, probability of fit 0.001), indicates that the use of a single regression line is not entirely justified (i.e., the scatter exceeds the purely analytical one). Close inspection of Fig. 7 indeed reveals that the distribution of data points is best accounted for by two regression lines, one through the upper four samples (358.11–358.13, 440.83–440.86, 564.92–564.93 and 640.13–640.16) and the second through the remaining lower six

605 samples (709.14–709.16, 709.17–709.19, 831.66–831.68, 953.28–953.31, 953.54–953.56 and
606 1093.00–1093.04). The regression lines are both statistically acceptable, with a probability of fit
607 >>0.05 (Fig. 7b and c), and yield mean sedimentation rates of 19.1±2.2 cm/ka and 19.5±3.5
608 cm/ka, overlapping within errors. These arguments indicate that Ar data from the ~358–
609 1093-mbsf interval records a relatively fast and constant mean sedimentation rate of ~19
610 cm/ka, with a possible break in between ~640 and ~709 mbsf (~17.4 and ~18.0 Ma,
611 respectively), characterized instead by a mean sedimentation rate as low as 9.9±2.6 cm/ka.
612 Coincidentally, an abrupt erosional contact was identified at 648.74 mbsf, and was taken as
613 the boundary between Lithostratigraphic Unit 9 and the underlying Lithostratigraphic Unit
614 10 (Fielding et al. 2008b). Furthermore, based on paleontological data (Fig. 7), such a fast
615 mean sedimentation rate should have persisted up to ~310–312 mbsf, where diatom data
616 indicate that sedimentation occurred within 15.50–15.70 Ma (Taviani et al. 2008). In light of
617 the large time interval encompassing the two identified intervals (i.e., ~1.5 and ~1.9 Ma) and
618 of available sedimentologic data (Fielding et al. 2008b), it is very unlikely however that
619 sedimentation was truly constant even within the 358–640- and 709–1096-mbsf intervals.
620 Rather results should be interpreted to indicate that departure (possible oscillations) from a
621 linear sedimentation rate, including true variations in deposition rate but also hiatuses,
622 should have been no longer than 2σ internal errors (Table 2), that is less than a few hundreds
623 of ka. This simple observation is intriguing since oscillations with periods of ≤400 ka
624 encompass those of orbital perturbations (Milankovitch cycles).

625 From a broader perspective, it is important to note that recent investigation on the AND-
626 2A sediment core (Warny et al. 2009) has revealed within the 310–312-mbsf interval a
627 palynological assemblage documenting a relatively short period of time during which
628 Antarctica became suddenly much warmer. This ice-proximal record of past Antarctic climate
629 suggesting that warming peaked at ~15.7 Ma, matches the Middle Miocene Climate
630 Optimum, a period (14–16 Ma) during which the Earth was warmer than today and which
631 was followed by a gradual cooling toward a more stable icehouse period (Zachos et al. 2001;
632 Shevenell et al. 2004). While it is beyond the scope of this work to draw general conclusions
633 about the paleoclimatic implications of the AND-2A core, a few prominent features of the
634 stratigraphic record need to be pointed out (Fig. 7): (1) the coincidence of the nearly
635 continuous Early to Middle Miocene record with a period during which glaciers in the area
636 are hypothesized to have been wet-based and possibly more erosive (e.g., Sudgen and
637 Denton 2004); (2) the concomitance of the warmer period (Warny et al. 2009) with the upper
638 termination of the nearly continuous Early to Middle Miocene section; (3) the coincidence of
639 the change in style and rate of deposition from the Middle Miocene onward with the
640 hypothesized shift from wet- to cold-based glaciers (~14 Ma – Sudgen and Denton 2004;
641 Lewis et al. 2007) and with a climate degradation on a global scale (e.g., Shevenell et al. 2004);
642 (4) the consistency of the condensed and discontinuous Middle Miocene to Recent record
643 with an environment close to the margin of a dynamic ice sheet (Naish et al. 2009; McKay et

al. 2009). The above arguments suggest that future research on the AND-2A sediment core have a strong potential to shed light on the apparent inconsistency between a scenario in which the East Antarctic Ice Sheet became stable and cold starting from about 14 Ma (Sudgen and Denton 2004; Lewis et al. 2007), and another in which the Antarctic Ice Sheets instead underwent important fluctuations over the past 13 Ma, with repetitive oscillations of ice-sheet extent (McKay et al. 2009).

On the basis of preliminary ^{40}Ar–^{39}Ar ages and available paleontological data, Acton et al. (2008a, b) correlated paleomagnetic data from the 328.52–581.34-mbsf interval with Chron C5Cn.1n (15.974–16.268 Ma) to Chron C5Cr (16.721–17.235 Ma). Polarity chron boundaries from the above mentioned interval yield ages that match within error those obtained from ^{40}Ar–^{39}Ar data, irrespective of the constants used in the calculation of Ar ages (Fig. 7 and Table 2). Below 581.34 mbsf however, interpretation of paleomagnetic data is more uncertain (Acton et al. 2008a, b), as the identified magnetozones may be either correlated with Chron C5Dn (17.235–17.533 Ma) to Chron C6n (18.748–19.772 Ma) or with Chron C5Dn to Chron C6An.1n (20.040–20.213 Ma), with polarity chron boundaries differing in age by as much as ~1.3 Ma (Fig. 7 and Table 2). Correlation of paleomagnetic data with Chrons C5Dn to C6n however would imply that volcanic materials from 709.14 mbsf down hole were reworked long before final deposition. Indeed, assuming a linear sedimentation rate between tie points, paleomagnetic data would yield ages that are significantly younger than those from radioisotopic data, even when full errors are taken into account (Table 2): ages extrapolated from paleomagnetic data are 0.43±0.40 Ma to 0.98±0.34 Ma and 0.54±0.31 Ma to 1.10±0.17 Ma younger than ^{40}Ar–^{39}Ar ages calculated using constants of Steiger and Jäger (1977) and those proposed by Kuiper et al. (2008), respectively. In light of petrographic data, of the alignment of ^{40}Ar–^{39}Ar age data in a depth vs. age diagram (Fig. 7), as well as of paleontologic and paleomagnetic data both independently suggesting a relatively fast mean sedimentation rate below ~300 mbsf down hole, such a long reworking time for the studied samples seems to be a very unlikely possibility. Correlation of paleomagnetic data below 581.34-mbsf with Chron C5Dn to Chron C6An.1n, would instead yield a better fit with radioisotopic ages. With the exception of sample 709.17–709.19, yielding an Ar age marginally yet significantly younger than that extrapolated from paleomagnetic data ($18.04\pm0.31_{(K)}$ Ma vs. 18.44 Ma, Table 2), the remaining samples yield Ar ages indistinguishable at the 2σ confidence level from those derived from paleomagnetic data (Table 2) extrapolated from bracketing tie points (samples 640.13–640.16, 709.14–709.16, 709.17–709.19, and 1093.00–1093.04) or using the nearest upper (sample 831.66–831.68) or lower tie-points (samples 953.28–953.31 and 953.54–953.56).

Concluding remarks and general implications

One of the main goals of the ANDRILL SMS Project was to recover an expanded stratigraphic record from the Middle Miocene, in order to fill the gap left by previous drill cores (ANDRILL MIS and Cape Roberts projects). The Middle Miocene (~16.0 to 11.6 Ma; Gradstein et al. 2004) is indeed a key time interval in the construction of modern Antarctic cryosphere. This period hosts the Middle Miocene climate transition (14.2–13.8 Ma), which followed the Middle Miocene Climate Optimum and represents one of the key steps in the Cenozoic climate cooling (Zachos et al. 2001; Shevenell et al. 2004; Zachos et al. 2008).

^{40}Ar–^{39}Ar laser analyses on volcanic rocks of the AND-2A core from the present study, in conjunction with petrographic data, reveal that the SMS project recovered as much as ≤230 m of Middle Miocene and as much as >780 m of Early Miocene. Results indicate that future chronostratigraphic work should concentrate in the ~128–358-mbsf interval of the core in order to improve chronological control of the AND-2A core corresponding to Middle Miocene. More significantly, data from the present study reveal that the ~358–1093-mbsf interval of the core, corresponding to the Early Miocene (from ~16.0 to ~20.1 Ma), yields a nearly continuous stratigraphic record, characterized by a relatively fast and a nearly constant mean sedimentation rate of ~19 cm/ka, with a possible break in between ~640 and ~709 mbsf. In light of available independent chronological constraints for the AND-2A core, such a style of sedimentation should have persisted up to ~310 mbsf, corresponding to the beginning of Middle Miocene. It is important to note, however, that the available stratigraphy of the area (e.g., Fielding et al. 2008a) along with sedimentologic data from the AND-2A core (Fielding et al. 2008b), suggest that sedimentation was not truly constant in that period. ^{40}Ar–^{39}Ar age data therefore should be interpreted to indicate that departure (possible oscillations) from a linear sedimentation rate did not exceed a few hundreds of ka.

Preservation of a relatively thick and nearly continuous Early to Middle Miocene sedimentary sequence underlying a condensed and discontinuous Middle Miocene to Recent section, is in line with and reinforce the model proposed by Fielding et al. (2008a) for the evolution of the Cenozoic Victoria Land Basin of the West Antarctic Rift System. According to Fielding et al. (2008a), the Victoria Land Basin during Early to Middle Miocene (23 to 13 Ma) underwent a phase of passive thermal subsidence, that occurred in between Early Rift and Main Rift phases (within 29–23 Ma), producing the Victoria Land Basin, and a Renewed Rift phase (13 Ma to Recent) that produced the Terror Rift. Indeed, an Early Miocene phase of passive subsidence can explain the nearly continuous stratigraphic record (Fielding et al. 2008b) and the constant and relatively fast mean sedimentation rate calculated here. A renewed rift phase (Middle Miocene to Recent) that produced the Terror Rift with erosion of its western boundary and a shift in the locus of sedimentation to the east, instead accounts for a condensed and discontinuous stratigraphic record in the upper portion of the core (<225 mbsf, <14 Ma).

Comparison with available geochronological data from volcanic deposits on land of the Erebus Volcanic Province, suggests that investigated volcanogenic products were supplied

721 from the south, possibly with source deposits becoming closer to the drill site at upper core
722 levels. As for the nearly continuous Early Miocene stratigraphic record, Ar data suggest
723 derivation from volcanic deposits of the "proto-Mount Morning", that is more or less from a
724 "point-source". This is consistent with the observation that during the Early Miocene, before
725 the construction of Minna Bluff (>13 Ma), there was no obstruction to ice flow or ocean
726 currents. Furthermore, this would imply that the front of the ice shelf (when and if present at
727 that time) would have had a pinning line at "proto-Mount Morning" or further south. Ice
728 flow or ocean currents were able to transport volcanic clasts from Mason Spur to the north
729 without obstruction from Minna Bluff up until at least the Late Miocene (~11.5 Ma).
730
731
732 **Acknowledgements** The journal reviews of S. Hemming and W. LeMasurier, and the
733 editorial handling by M.A. Clynne are gratefully acknowledged. G.D.V. is indebted to W.
734 McIntosh, who kindly provided the fluence monitor Fish Canyon sanidine. The ANDRILL
735 Program is a multinational collaboration between the Antarctic programs of Germany, Italy,
736 New Zealand and United States. Antarctica New Zealand is the project operator and
737 developed the drilling system in collaboration with Alex Pyne at Victoria University of
738 Wellington and Webster Drilling and Exploration Ltd. Antarctica New Zealand supported
739 the drilling team at Scott Base; Raytheon Polar Services Corporation supported the science
740 team at McMurdo Station and the Crary Science and Engineering Centre. The ANDRILL
741 Science Management Office at the University of Nebraska-Lincoln provided science planning
742 and operational support. Scientific studies are jointly supported by the US National Science
743 Foundation (NSF), NZ Foundation for Research, Science and Technology (FRST), the Italian
744 Antarctic Research Programme (PNRA), the German Research Foundation (DFG) and the
745 Alfred Wegener Institute (AWI) for Polar and Marine Research. The Ar–Ar laserprobe facility
746 was funded by the PNRA and the CO_2 laser system by the Consiglio Nazionale delle
747 Ricerche.
748
749
750 **References**
751
752 Acton G, Crampton J, Di Vincenzo G, Fielding CR, Florindo F, Hannah M, Harwood D,
753 Ishman S, Johnson K, Covane L, Levy R, Lum B, Marcano MC, Mukasa S, Ohneiser C,
754 Olney M, Riesselman C, Sagnotti L, Stefano C, Strada E, Taviani M, Tuzzi E, Verosub KL,
755 Wilson GS, Zattin M (2008a) Preliminary integrated chronostratigraphy of the AND-2A
756 core, ANDRILL Southern McMurdo Sound Project. In: Harwood DM, Florindo F,
757 Talarico F, Levy RH (eds) Studies from the ANDRILL, Southern McMurdo Sound Project,
758 Antarctica. Terra Antart 15 (in press)

759 Acton G, Florindo F, Jovane L, Lum B, Ohneiser C, Sagnotti L, Strada E, Verosub KL, Wilson
760 GS (2008b) Palaeomagnetism of the AND-2A Core, ANDRILL Southern McMurdo Sound
761 Project, Antarctica. In: Harwood DM, Florindo F, Talarico F, Levy RH (eds) Studies from
762 the ANDRILL, Southern McMurdo Sound Project, Antarctica. Terra Antart 15 (in press)
763 Bachmann O, Oberli F, Dungan MA, Meier M, Mundil R, Fischer H (2007) $^{40}Ar/^{39}Ar$ and U–
764 Pb dating of the Fish Canyon magmatic system, San Juan Volcanic field, Colorado:
765 evidence for an extended crystallization history. Chem Geol 236:134–166
766 Barrett PJ (1987) Oligocene sequence cored at CIROS-1, western McMurdo Sound. New
767 Zealand Antarctic Record 7:1–17
768 Barrett PJ (2007) Cenozoic climate and sea level history from glacimarine strata off the
769 Victoria Land coast, Cape Roberts Project, Antarctica. In: Hambrey MJ, Christoffersen P,
770 Glasser NF, Hubbart B (eds) Glacial Processes and Products. International Association of
771 Sedimentologists Special Publication 39:259–287
772 Cooper AK, Davey FJ, Behrendt JC (1987) Seismic stratigraphy and structure of the Victoria
773 Land Basin, western Ross Sea, Antarctica. In: Cooper AK, Davey FJ (eds) The Antarctic
774 Continental Margin: Geology and Geophysics of the Western Ross Sea, 5b. Circum-Pacific
775 Council for Energy and Natural Resources Earth Science Series 27–76
776 Cooper AF, Lotte JA, Coulter RF, Nelson Eby G, McIntosh WC (2007) Geology,
777 geochronology and geochemistry of a basaltic volcano, White Island, Ross Sea,
778 Antarctica. J Volcanol Geoth Res 165:189–216. doi:10.1016/j.jvolgeores.2007.06.003
779 Del Carlo P, Panter KS, Bassett K, Bracciali L, Di Vincenzo G, Rocchi S (2009) Evidence for
780 local volcanic sources in the upper lithostratigraphic unit of ANDRILL AND-2A core
781 (Southern McMurdo Sound, Antarctica) and implications for paleoenvironment and
782 subsidence in the western Victoria Land basin. Global Planet Change. doi:
783 10.1016/jgloplacha.2009.09.002
784 Di Vincenzo G, Skála R (2009) $^{40}Ar–^{39}Ar$ laser dating of tektites from the Cheb Basin (Czech
785 republic): Evidence for coevality with moldavites and influence of the dating standard on
786 the age of the Ries impact. Geochim Cosmochim Acta 73:493–513. doi:
787 10.1016/j.gca.2008.10.002
788 Dibble RR, Kyle PR, Rowe CA (2008) Video and seismic observations of Strombolian
789 eruptions at Erebus volcano, Antarctica. J Volcanol Geoth Res 177:619–634. doi:
790 10.1016/j.jvolgeores.2008.07.020
791 Esser RP, McIntosh WC, Heizler MT, Kyle PR (1997) Excess argon in melt inclusions in zero-
792 age anothoclase feldspar from Mt. Erebus, Antarctica as revealed by the $^{40}Ar/^{39}Ar$
793 method. Geochim Cosmochim Acta 61:3789–3801
794 Esser RP, Kyle PR, McIntosh WC (2004) $^{40}Ar/^{39}Ar$ dating of the eruptive history of Mount
795 Erebus, Antarctica: volcano evolution. Bull Volcanol 66:671–686. doi: 10.1007/s00445-004-
796 0354-x

797 Fargo AJ, McIntosh WC, Dunbar NW, Wilch TI (2008) ^{40}Ar–^{39}Ar geochronology of Minna
798 Bluff, Antarctica: timing of Mid-Miocene glacial erosional events within the Ross
799 Embayment. Eos Trans. AGU, 89(53), Fall Meet Suppl, Abstract V13C-2127
800 Fielding CR, Whittaker J, Henrys SA, Wilson TJ, Naish TR (2008a) Seismic facies and
801 stratigraphy of the Cenozoic succession in McMurdo Sound, Antarctica: implications for
802 tectonic, climate and glacial history. Palaeogeogr Palaeocl 260:8–29. doi:
803 10.1016/j.palaeo.2007.08.016
804 Fielding CR, Atkins CB, Bassett KN, Browne GH, Dunbar GB, Field BD, Frank TD, Panter KS,
805 Pekar SF, Krissek LA, Passchier S (2008b) Sedimentology and stratigraphy of the AND-
806 2A core, ANDRILL Southern McMurdo Sound, Project, Antarctica. In: Harwood DM,
807 Florindo F, Talarico F, Levy RH (eds) Studies from the ANDRILL, Southern McMurdo
808 Sound Project, Antarctica. Terra Antart 15 (in press)
809 Florindo F, Harwood D, Levy R, SMS Project Science Team (2008) ANDRILL's success during
810 the 4th International Polar Year. Scientific Drilling, 6, July 2008, p. 29–31
811 Flower BP, Kennett JP (1994) The middle Miocene climatic transition: East Antarctic ice sheet
812 development, deep ocean circulation and global carbon cycling. Palaeogeogr Palaeocl
813 108:537–555
814 Gamble JA, Barrett PJ, Adams CJ (1986) Basaltic clasts from Unit 8. Bulletin of New Zealand
815 DSIR 237:145–152
816 Gradstein FM, Ogg JG, Smith AG (2004) A Geologic Time Scale 2004. Cambridge University
817 Press, Cambridge, United Kingdom, 610 pp
818 Harwood DM, Florindo F, Talarico F, Levy RH, Acton G, Fielding C, Panter K, Paulsen T,
819 Taviani M (2008) Synthesis of the Initial Scientific Results of the ANDRILL Southern
820 McMurdo Sound Project, Victoria Land Basin, Antarctica. In: Harwood DM, Florindo F,
821 Talarico F, Levy RH (eds) Studies from the ANDRILL, Southern McMurdo Sound Project,
822 Antarctica. Terra Antart 15 (in press)
823 Harpel CJ, Kyle PR, Esser RP, McIntosh WC, Caldwell DA (2004) $^{40}Ar/^{39}Ar$ dating of the
824 eruptive history of Mount Erebus, Antarctica: summit flows, tephra, and caldera collapse.
825 Bull Volcanol 66:687–702. doi: 10.1007/s00445-004-0349-7
826 Holbourn A, Kuhnt W, Schulz M, Flores J-A, Andersen N (2007) Orbitally-paced climate
827 evolution during the Middle Miocene "Monterey" carbon-isotope excursion. Earth Planet
828 Sci Lett 261:534–550. doi:10.1016/j.epsl.2007.07.026
829 Johnston L, Wilson GS, Gorman AR, Henrys SA, Horgan H, Clark R, Naish TR (2008)
830 Cenozoic basin evolution beneath the southern McMurdo Ice Shelf, Antarctica. Global
831 Planet Change 62:61–76. doi: 10.1016/j.gloplacha.2007.11.004
832 Jourdan F, Renne PR (2007) Age calibration of the Fish Canyon sanidine $^{40}Ar/^{39}Ar$ dating
833 standard using primary K–Ar standard. Geochim Cosmochim Acta 71:387–402.
834 doi:10.1016/j.gca.2006.09.002

835 Kelly PJ, Kyle PR, Dunbar NW, Sims KWW (2008) Geochemistry and mineralogy of the
836 phonolite lava lake, Erebus volcano, Antarctica: 1972-2004 and comparison with older
837 lavas. J Volcanol Geoth Res 177:589–605. doi: 10.1016/j.jvolgeores.2007.11.025
838 Koppers AAP, Staudigel H, Wijbrans JR (2000) Dating crystalline groundmass separates of
839 altered Cretaceous seamount basalts by the $^{40}Ar/^{39}Ar$ incremental heating technique.
840 Chem Geol 166:139–158
841 Krumrei TV, Villa IM, Marks, MAW, Markl G (2006) A $^{40}Ar/^{39}Ar$ and U/Pb isotopic study of
842 the Ilímaussaq complex, South Greenland: implications for the ^{40}K decay constant and for
843 the duration of magmatic activity in a peralkaline complex. Chem Geol 227:258–273. doi:
844 10.1016/j.chemgeo.2005.10.004
845 Kuiper KF, Deino A, Hilgen FJ, Krijgsman W, Renne PR, Wijbrans JR (2008) Synchronizing
846 rock clocks of Earth history. Science 320:500–504. doi: 10.1126/science.1154339
847 Kyle PR (1990a) McMurdo Volcanic Group – Introduction. In: LeMasurier WE, Thomson JW
848 (eds) Volcanoes of the Antarctic Plate and Southern Oceans. Antarctic Research Series 48,
849 American Geophysical Union, Washington DC, 19–25
850 Kyle PR (1990b) Erebus Volcanic Province - Summary. In: LeMasurier WE, Thomson JW (eds)
851 Volcanoes of the Antarctic Plate and Southern Oceans. Antarctic Research Series 48,
852 American Geophysical Union, Washington DC, 81–135
853 Kyle PR, Cole, JW (1974) Structural control of volcanism in the McMurdo Volcanic Group,
854 Antarctica. Bull Volcanol 38:16–25
855 Kyle PR, Muncy HL (1989) Geology and geochronology of McMurdo Volcanic Group rocks in
856 the vicinity of Lake Morning, McMurdo Sound, Antarctica. Antarct Sci 1:345–350
857 Kyle PR, Moore JA, Thirlwall MF (1992) Petrologic evolution of anorthoclase phonolite lavas
858 at Mount Erebus, Ross Island, Antarctica. J Petrol 33:849–875
859 Lawrence KP, Tauxe L, Staudigel H, Constable CG, Koppers A, McIntosh W, Johnson CL
860 (2009) Paleomagnetic field properties at high southern latitude. Geochem Geophy Geosy
861 (G^3) 10, doi:10.1029/2008GC002072
862 Lewis AR, Marchant DR, Ahworth AC, Hemming SR, Machlus ML (2007) Major middle
863 Miocene global climate change: evidence from East Antarctica and the Transantarctic
864 Mountains. Geol Soc Am Bull 119:1449–1461. doi: 10.1130B26134.1
865 Marchant DR, Denton GH, Swisher III CC, Potter Jr N (1996) Late Cenozoic Antarctic
866 paleoclimate reconstructured from volcanic ashes in the Dry Valleys region of southern
867 Victoria Land. Geol Soc Am Bull 108:181–194
868 Martin AP, Cooper AF, Dunlap WJ (2009) Geochronology of Mount Morning, Antarctica:
869 two-phase evolution of a long-lived trachyte-basanite-phonolite eruptive center. Bull
870 Volcanol. doi: 10.1007/s00445-009-0319-1
871 McIntosh WC (1998) $^{40}Ar/^{39}Ar$ geochronology of volcanic clasts and pumice in CRP-1 core,
872 Cape Roberts, Antarctica. Terra Antart 5:683–690

McIntosh WC (2000) $^{40}Ar/^{39}Ar$ geochronology of tephra and volcanic clasts in CRP-2A, Victoria Land Basin, Antarctica. Terra Antart 7:621–630

McKay R, Browne G, Carter L, Cowan E, Bunbar G, Krissek L, Naish T, Powell R, Reed J, Talarico F, Wilch T (2009) The stratigraphic signature of the late Cenozoic Antarctica Ice Sheets in the Ross Embayments. Geol Soc Am Bull 121:1537–1561. doi: 10.1130/B26540.1

Min K, Mundil R, Renne PR, Ludwig KR (2000) A test for systematic errors in $^{40}Ar/^{39}Ar$ geochronology through comparison with U–Pb analysis of a 1.1 Ga rhyolite. Geochim Cosmochim Acta 64:73–98

Naish T, Powell R, Levy R, ANDRILL-MIS Science Team (2007) Background to the ANDRILL McMurdo Ice Shelf project (Antarctica) and initial science volume. Terra Antart 14:121–130

Naish T, Powell R, Levy R, Wilson G, Scherer R, Talarico F, Krissek L, Niessen F, Pompilio M, Wilson T, Carter L, DeConto R, Huybers P, McKay R, Pollard D, Ross J, Winter D, Barrett P, Browne G, Cody R, Cowan E, Crampton J, Dunbar G, Dunbar N, Florindo F, Gebhardt C, Graham I, Hannah M, Hansaraj D, Harwood D, Helling D, Henrys S, Hinnov L, Kuhn G, Kyle P, Läufer A, Maffioli P, Magens D, Mandernack K, McIntosh W, Millan C, Morin R, Ohneiser C, Paulsen T, Persico D, Raine I, Reed J, Riesselman C, Sagnotti L, Schmitt D, Sjunneskog C, Strong P, Taviani M, Vogel S, Wilch T, Williams T (2009) Obliquity-paced Pliocene West Antarctic ice sheet oscillations. Nature 458:322–328. doi: 10.1038/nature0867

Panter KS, Talarico F, Bassett K, Del Carlo P, Field B, Frank T, Hoffman S, Kuhn G, Reichelt L, Sandroni S, Tavini M, Bracciali L, Cornamusini G, von Eynatten H, Rocchi R (2008) Petrologic and Geochemical Composition of the AND-2A Core, ANDRILL Southern McMurdo Sound Project, Antarctica. In: Harwood DM, Florindo F, Talarico F, Levy RH (eds), Studies from the ANDRILL, Southern McMurdo Sound Project, Antarctica. Terra Antart 15 (in press)

Paulsen TS, Wilson TJ (2009) Structure and age of volcanic fissures on Mount Morning: a new constraint on Neogene to contemporary stress in the West Antarctic Rift, southern Victoria Land, Antarctica. Geol Soc Am Bull 121:1071–1088. doi: 10.1130/B26333.1

Pompilio M, Dunbar N, Gebhardt AC, Helling D, Kuhn G, Kyle P, McKay R, Talarico F, Tulaczyk S, Vogel S, Wilch T, ANDRILL-MIS Science Team (2007) Petrology and geochemistry of the AND-1B Core, ANDRILL McMurdo Ice Shelf Project, Antarctica. Terra Antart 14, 255–288

Renne, PR, Swisher CC, Deino AL, Karner DB, Owens TL, DePaolo DJ (1998) Intercalibrations of standards, absolute ages and uncertainties in $^{40}Ar/^{39}Ar$ dating. Chem Geol 145:117–152

Rilling SE, Mukasa SB, Wilson TJ, Lawver LA (2007) $^{40}Ar–^{39}Ar$ age constraints on volcanism and tectonism in the Terror Rift of the Ross Sea, Antarctica. In: Cooper AK, Raymond CR (eds) Antarctica: a keystone in a changing word – Online Proceedings of the 10th ISAES, USGS Open-File Report 2007–1047, Short Research Paper 092, 4pp

912 Schoene B, Crowley JL, Condon DJ, Schmitz MD, Bowring SA (2006) Reassessing the uranium
913 decay constants for geochronology using ID-TIMS U–Pb data. Geochim Cosmochim Acta
914 70:426–445. doi: 10.1016/j.gca.2005.09.007
915 Shevenell AE, Kennett JP, Lea DW (2004) Middle Miocene Southern Ocean cooling and
916 Antarctic cryosphere expansion. Science 305:1766–1770
917 Steiger RH, Jäger E (1977) Subcommission on Geochronology: convention on the use of decay
918 constants in geo- and cosmochronology. Earth Planet Sci Lett 36:359–362
919 Sudgen D, Denton G (2004) Cenozoic landscape evolution of the Convoy Range to Mackay
920 Glacier area, Transantarctic Mountains: onshore to offshore synsthesis. Geol Soc Am Bull
921 116:840–857 doi: 10.1130/B25356.1
922 Tauxe L, Gans P, Mankinen EA (2004) Paleomagnetism and $^{40}Ar/^{39}Ar$ ages from volcanics
923 extruded during the Matuyama and Brunhes Chrons near McMurdo Sound, Antarctica.
924 Geochem Geophy Geosy (G^3) 5, doi:10.1029/2003GC000656
925 Taviani M, Hannah M, Harwood DM, Ishman SE, Johnson K, Olney M, Riesselman C, Tuzzi
926 E, Askin R, Beu AG, Blair S, Cantarelli V, Ceregato A, Corrado S, Mohr B, Nielsen SHH,
927 Persico D, Petrushak S, Raine JI, Warny S (2008) Palaeontologic Characterization of the
928 AND-2A Core, ANDRILL Southern McMurdo Sound Project, Antarctica. In: Harwood
929 DM, Florindo F, Talarico F, Levy RH (eds) Studies from the ANDRILL, Southern
930 McMurdo Sound Project, Antarctica. Terra Antart 15 (in press)
931 Van der Wateren FM, Cloetingh SAPL (1999) Feedbacks of lithosphere dynamics and
932 environmental change of the Cenozoic west Antarctic rift system. Global Planet Change
933 23:1–24
934 Warny S, Askin RA, Hannah MJ, Mohr BAR, Raine JI, Harwood DM, Florindo F, SMS Science
935 Team (2009) Palynomorphs from a sediment core reveal a sudden remarkably warm
936 Antarctica during the Middle Miocene. Geology 37:955–958. doi: 10.1130/G30139A.1
937 Wilch TI, Lux DR, Denton GH, McIntosh WC (1993) Minimal Pliocene-Pleistocene uplift of
938 the dry valleys sector of the Transantarctic Mountains: a key parameter in ice-sheet
939 reconstructions. Geology 21:841–844
940 Wilson G, Levy R, Browne G, Cody R, Dunbar N, Florindo F, Henys S, Graham I, McIntosh
941 W, McKay R, Naush T, Ohneisr C, Powell R, Ross J, Sagnotti L, Schere R, Sjunneskog C,
942 Strong CP, Taviani M, Winter D, ANDRILL-MIS Science Team (2007) Preliminary
943 integrated chronostratigraphy of the AND-1B core, ANDRILL McMurdo Ice Shelf Project,
944 Antarctica. Terra Antart 14:297–316
945 Wilson TJ (1995) Cenozoic transtension along the Transantarctic Mountains west Antarctic rift
946 boundary, southern Victoria Land, Antarctica. Tectonics 14:531–545
947 Wilson TJ (1999) Cenozoic structural segmentation of the Transantarctic Mountains rift flank
948 in southern Victoria Land. Global Planet Change 23:105–127
949 Wilson TJ, Demosthenous CM (2000) SAR-based mapping of glaciated volcanic terrain: the
950 Erebus Volcanic Province, Antarctica. Canadian Journal of Remote Sensing 26:142–158

951 Wilson TJ, Paulsen T, Wilch TI (2003) Structural control on Neogene-Quaternary volcanism in
952 the Transantarctic Mountains, southern Victoria Land, Antarctica, EGS-AGU-EUG 2003
953 Joint Assembly, Volume 5: Nice, France, 14357 p
954 Wright-Grassham AC (1987) Volcanic geology, mineralogy, and petrogenesis of the
955 Discovery Volcanic Subprovince, Southern Victoria Land, Antarctica. PhD thesis, New
956 Mexico Institute of Mining and Technology, Socorro
957 Zachos J, Pagani M, Sloan L, Thomas E, Billups K (2001) Trends, rhythms, and aberrations in
958 global climate 65 Ma to Present. Nature 292:686–693
959 Zachos JC, Dickens GR, Zeebe RE (2008) An early Cenozoic perspective on greenhouse
960 warming and carbon-cycle dynamics. Nature 451:279–283. doi: 10.1038/nature06588
961

961 **Figure captions**
962
963 **Fig. 1** Satellite image of the McMurdo Sound area showing the location of the ANDRILL SMS
964 (AND-2A) drill site and previous drill sites. Inset **b** has been redrawn and modified after
965 Fielding et al. (2008a).
966
967 **Fig. 2** Cumulative probability and ranked distribution of ages from total fusion experiments
968 on alkali feldspar separates. Bars are 2σ analytical errors. Uncertainties on the error-weighted
969 mean ages also include the error in the *J* values.
970
971 **Fig. 3** Age release and K/Ca spectra of groundmass and feldspar separates. Box eights
972 indicate the 2σ analytical error. Uncertainties on total gas and error-weighted mean ages are
973 2σ internal error.
974
975 **Fig. 4** Age (Ma) vs. Cl/K (derived from neutron-produced $^{38}Ar_{Cl}/^{39}Ar_K$ ratios) diagram for
976 data from step-heating and total fusion analyses on alkali feldspar of clast 8.88–9.02. Note the
977 well-defined positive correlation suggesting that the spread of data can be accounted for by a
978 binary mixture.
979
980 **Fig. 5** Isochron plot ($^{36}Ar/^{40}Ar$ vs. $^{39}Ar/^{40}Ar$ three-isotope correlation diagram) for total
981 fusion analyses on alkali feldspar from tephra layer 640.13–640.16.
982
983 **Fig. 6** Comparison of published K–Ar and ^{40}Ar–^{39}Ar ages for volcanic rocks of the Erebus
984 Volcanic Province (**a**-**b**-**c**-**d**) with ^{40}Ar–^{39}Ar ages for volcanogenic products from the AND-2A
985 core (this study) and previous drill cores (**e**). Error bars for all ^{40}Ar–^{39}Ar ages are 2σ internal
986 uncertainties. ^{40}Ar–^{39}Ar ages are relative to an age of 28.03 Ma for the FCs standard (Jourdan
987 and Renne 2007), with the exception of: (1) ages from Rilling et al. (2007) recalculated
988 assuming an age of 28.26 Ma for the FCT-3 standard (Di Vincenzo and Skála, 2009); (2) ages
989 from Wilch et al. (1993) recalculated assuming an age of 523.1 Ma for the Mmhb-1 standard
990 (Renne et al. 1998); (3) ages from Tauxe et al. 2004 recalculated assuming an age of 28.34 Ma
991 for the TCs standard (Renne et al. 1998). Error bars for K–Ar ages refer to the uncertainties
992 originally reported by the authors. ^{40}Ar–^{39}Ar ages are from: Wilch et al. (1993); Marchant et al
993 (1996); McIntosh (1998, 2000); Esser et al (2004); Harpel et al. (2004) Tauxe et al 2004; Cooper
994 et al. (2007); Lewis et al. (2007); Rilling et al. (2007); Wilson et al. (2007); Kelly et al. (2008); Del
995 Carlo et al. (2009); Lawrence et al. (2009); Martin et al. (2009); Paulsen and Wilson (2009). K–
996 Ar ages are from Kyle and Muncy (1989) and those listed in Kyle 1990. Ellipses in **d** show age
997 intervals based on new ^{40}Ar–^{39}Ar analyses recently reported for Minna Bluff (Fargo et al.
998 2008). See Fig. 1 for localities. LSU, Lithostratigraphic Unit.
999

1000 **Fig. 7** Depth vs. age diagram of volcanic samples from the AND-2A core investigated in this
1001 study. Ages are listed in Table 2. **a**-**b** ages calculated using the IUGS recommended constants
1002 (Steiger and Jäger 1977) and an age of 28.03 Ma for the fluence monitor FCs (Jourdan and
1003 Renne, 2007). Error bars are 2σ full uncertainties. Results of least squares fit through samples
1004 358.11–358.13 to 1093.00–1093.04 (**a**) and through samples 358.11–358.13 to 640.13–640.16 and
1005 samples 709.14–709.16 to 1093.00–1093.04 (**b**) using 2σ internal errors are also shown. **c** ages
1006 calculated using a ^{40}K total decay constants of (5.463±0.214) $\cdot 10^{-10}$ a^{-1} (Min et al. 2000) and an
1007 age for FCs of 28.201±0.046 Ma (±2σ, incorporating all sources of error; Kuiper et al. 2008).
1008 Error bars are 2σ full uncertainties. Ages from paleomagnetic and paleontological data, and
1009 ages based on Sr isotope compositions of shell fragments are from Acton et al. (2008a, b) and
1010 Taviani et al. (2009). Peak of climatic warning based on palynological signal in the AND-2A
1011 core from Warny et al. (2009). GPTS, Geological Polarity Time Scale (Gradstein et al. 2004).
1012 LSU, Lithostratigraphic Unit.

Table 1 Samples from the AND-2A core analyzed by the ^{40}Ar–^{39}Ar dating method

sample (depth interval in mbsf)	LSU	type	lithology	deposit type	degree of reworking	phase analyzed
8.88–9.02[a]	1.1	lava clast	phonolite[b]	bagged sample[d]	strongly reworked	alkali feldspar
10.22–10.44	1.2	lava clast	basanite[b]	bagged sample[d]	strongly reworked	groundmass
12.23–12.41	1.2	lava clast	hawaiite[b]	bagged sample[d]	strongly reworked	groundmass
18.03–18.25	1.2	lava clast	hawaiite[b]	bagged sample[d]	strongly reworked	groundmass
18.69–18.73	1.2	lava clast	tephrite[b]	bagged sample[d]	strongly reworked	groundmass
127.50–127.52	4	lava clast	felsic[c]	diamictite	strongly reworked	alkali feldspar
129.96–129.97	4	lava clast	basaltic[c]	diamictite	strongly reworked	plagioclase
358.11–358.13	7	lava clast	intermediate[c]	diamictite	strongly reworked	groundmass
440.83–440.86	8.1	lava clast	intermediate[c]	mudstone	strongly reworked	alkali feldspar
564.92–564.93	8.2	lava clast	felsic[c]	conglomerate	strongly reworked	alkali feldspar
640.13–640.16	9	pumice	felsic[c]	lapilli tuff	primary	alkali feldspar
709.14–709.16	10	pumice	felsic[c]	tuffaceous sandstone	moderately reworked	alkali feldspar
709.17–709.19	10	pumice	felsic[c]	tuffaceous sandstone	moderately reworked	alkali feldspar
831.66–831.68	11	pumice	felsic[c]	tuffaceous silty-sandstone	nearly primary	alkali feldspar
953.28–953.31	12	pumice	felsic[c]	tuffaceous fine muddy sandstone	nearly primary	alkali feldspar
953.54–953.56	12	pumice	felsic[c]	tuffaceous fine muddy sandstone	nearly primary	alkali feldspar
1093.00–1093.04	14	pumice	felsic[c]	tuffaceous sandstone	nearly primary	alkali feldspar

LSU, Lithostratigraphic Unit. [a] sample 8.88–9.02 corresponds to sample 8.88–9.02a in Del Carlo et al. (2009). [b] lithology determined from whole-rock geochemistry (see Del Carlo et al. 2009). [c] lithology determined from mineralogy/mineral chemistry. [d] stratigraphic relationships not recognizable.

Table 2 Summary of ^{40}Ar–^{39}Ar results from samples of the AND-2A core. Analytical procedures are described in the Electronic Supplementary Material

sample (mbsf)	phase analyzed	extraction technique	total number of analyses	age (Ma)[a]	±2σ[b]	±2σ[c]	type	MSWD	P	number of analyses	**age (Ma)[d]**	**±2σ[e]**	**±2σ[f]**	ages from polarity chron boundaries[g]	ages from polarity chron boundaries[h]
8.88–9.02	alkali feldspar	SH and TF (CO_2 laser)	14	≤0.080	–	–	3-isotope correlation diagram	–	–	14	**≤0.080**	**–**	**–**	–	–
10.22–10.44	groundmass	SH (Nd:YAG laser)	10	0.692	0.038	0.040	EWM	0.59	0.62	4	**0.696**	**0.038**	**0.040**	–	–
12.23–12.41	groundmass	SH (Nd:YAG laser)	10	0.793	0.063	0.066	EWM	0.10	0.75	2	**0.798**	**0.063**	**0.065**	–	–
18.03–18.25	groundmass	TF (Nd:YAG laser)	1	16.1	2.2	2.2	TF	–	–	1	**16.2**	**2.2**	**2.2**	–	–
18.69–18.73	groundmass	TF (Nd:YAG laser)	1	9.5	1.2	1.2	TF	–	–	1	**9.6**	**1.2**	**1.2**	–	–
127.50–127.52	alkali feldspar	TF (CO_2 laser)	12	11.363	0.072	0.20	EWM	1.00	0.44	11	**11.432**	**0.072**	**0.091**	–	–
129.96–129.97	plagioclase	SH (CO_2 laser)	8	11.43	0.46	0.50	EWM	0.63	0.73	8	**11.50**	**0.46**	**0.48**	–	–
358.11–358.13	groundmass	SH (Nd:YAG laser)	13	15.91	0.14	0.29	EWM	2.2	0.083	4	**16.01**	**0.14**	**0.17**	15.85	–
440.83–440.86	alkali feldspar	TF (CO_2 laser)	5	16.54	0.34	0.43	EWM	0.74	0.39	2	**16.64**	**0.34**	**0.37**	16.48	–
564.92–564.93	alkali feldspar	TF (CO_2 laser)	16	17.10	0.14	0.31	EWM	1.4	0.15	16	**17.20**	**0.14**	**0.17**	17.14	–
640.13–640.16	alkali feldspar	TF (CO_2 laser)	17	17.39	0.11	0.30	EWM	1.4	0.14	17	**17.50**	**0.11**	**0.14**	17.36	17.52
709.14–709.16	alkali feldspar	TF (CO_2 laser)	10	18.15	0.18	0.34	EWM	0.95	0.45	6	**18.26**	**0.18**	**0.21**	17.50	18.44
709.17–709.19	alkali feldspar	TF (CO_2 laser)	10	17.93	0.28	0.40	EWM	0.83	0.51	5	**18.04**	**0.28**	**0.31**	17.50	18.44
831.66–831.68	alkali feldspar	TF (CO_2 laser)	15	18.71	0.12	0.33	EWM	0.93	0.53	15	**18.82**	**0.12**	**0.15**	18.18	18.93
953.28–953.31	alkali feldspar	TF (CO_2 laser)	15	19.44	0.12	0.34	EWM	1.06	0.39	15	**19.56**	**0.12**	**0.15**	18.51	19.72
953.54–953.56	alkali feldspar	TF (CO_2 laser)	12	19.49	0.14	0.34	EWM	1.11	0.35	12	**19.61**	**0.14**	**0.17**	18.51	19.72
1093.00–1093.04	alkali feldspar	TF (CO_2 laser)	18	20.01	0.12	0.35	EWM	1.13	0.32	17	**20.13**	**0.12**	**0.15**	<19.47	<20.16

P, probability of fit. SH, step-heating analysis. TF, total fusion analysis. EWM, error-weighted mean. [a] ages calculated using the IUGS recommended constants (Steiger and Jäger 1977) and an age of 28.03 Ma for the fluence monitor FCs (Jourdan and Renne 2007). [b] ±2σ internal error. [c] ±2σ full error. [d] ages calculated using a ^{40}K total decay constants of $(5.463\pm0.214) \cdot 10^{-10}$ a^{-1} (Min et al. 2000) and an age for FCs of 28.201±0.046 Ma (±2σ, incorporating all sources of error; Kuiper et al. 2008). [e] ±2σ internal error. [f] ±2σ full error. [g] ages extrapolated assuming a linear deposition rate between polarity chron boundaries given in Acton et al. (2008a, b) and based on chron ages from GPTS of Gradstein et al. (2004). The last 23 Ma of the GPTS of Gradstein et al. (2004) is orbitally tuned with 40 ka accuracy (see also text). [h] same as in column [g], alternate interpretation. In bold preferred ages and associated errors.

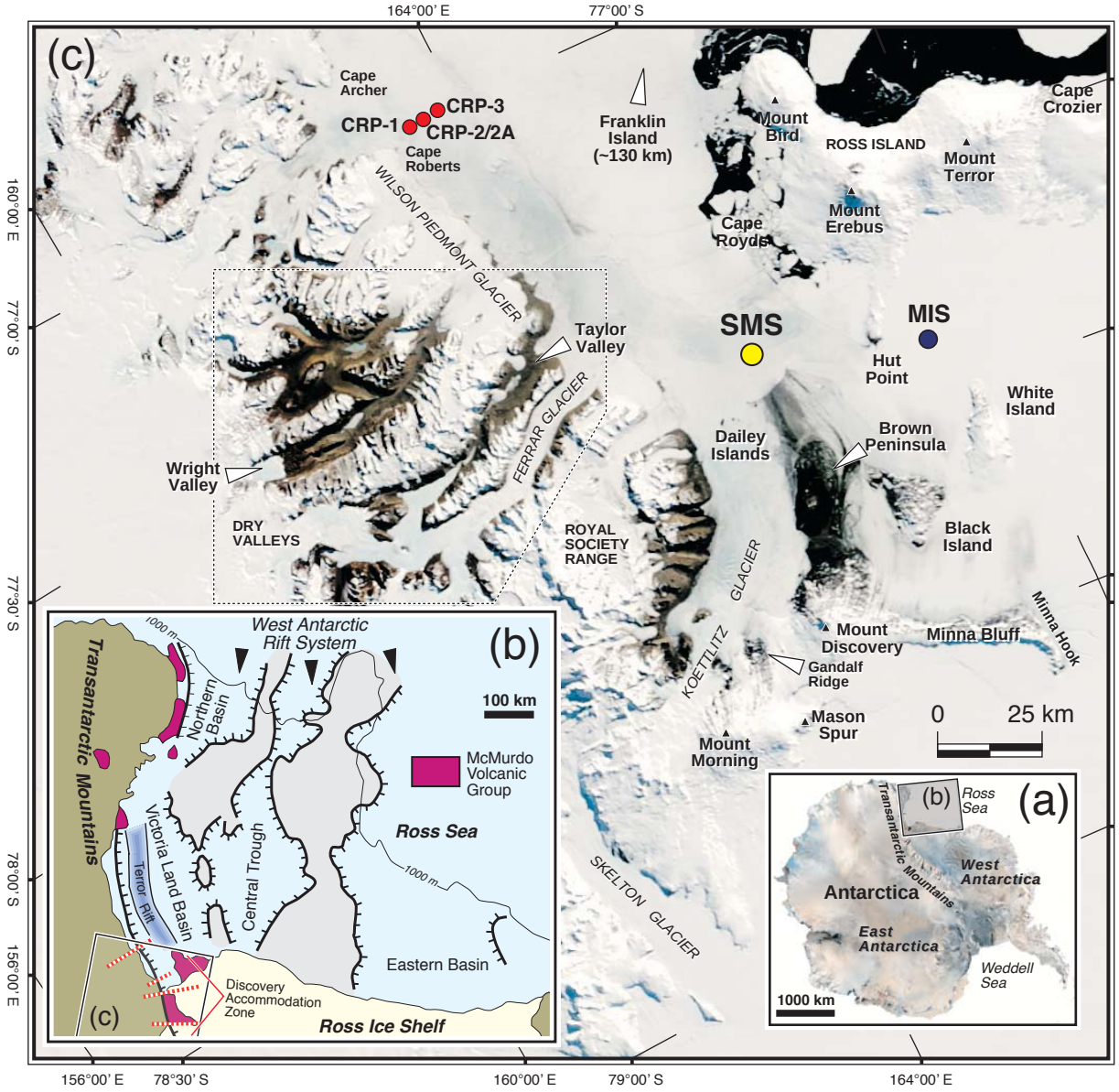
(c)
164°00' E
77°00' S
77°30' S
160°00' E
77°00' S
78°00' S
77°30' S
78°30' S
168°00' E
79°00' S
156°00' E
78°30' S
160°00' E
79°00' S
164°00' E
Cape Archer
CRP-3
CRP-1
CRP-2/2A
Cape Roberts
Franklin Island (~130 km)
Mount Bird
ROSS ISLAND
Cape Crozier
Mount Terror
Mount Erebus
Cape Royds
WILSON PIEDMONT GLACIER
Taylor Valley
SMS
MIS
Hut Point
White Island
Dailey Islands
Brown Peninsula
FERRAR GLACIER
Wright Valley
DRY VALLEYS
ROYAL SOCIETY RANGE
Black Island
GLACIER
KOETTLITZ
Mount Discovery
Minna Bluff
Minna Hook
Gandalf Ridge
Mason Spur
Mount Morning
0
25 km
SKELTON GLACIER
(b)
West Antarctic Rift System
100 km
Transantarctic Mountains
Northern Basin
McMurdo Volcanic Group
Victoria Land Basin
Terror Rift
Central Trough
Ross Sea
1000 m
Eastern Basin
(c)
Discovery Accommodation Zone
Ross Ice Shelf
(a)
Ross Sea
Transantarctic Mountains
West Antarctica
Antarctica
East Antarctica
Weddell Sea
1000 km

Fig. 1

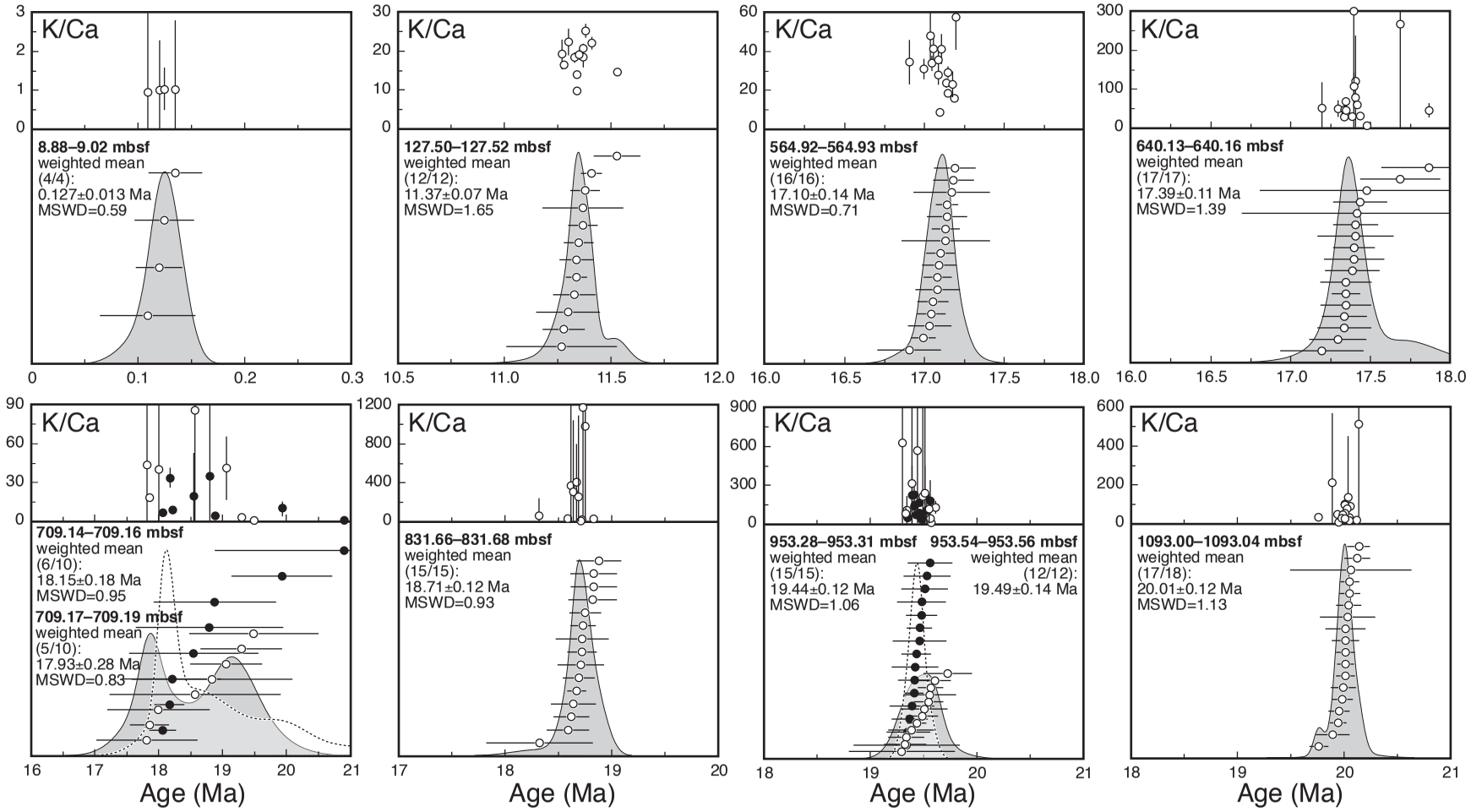
K/Ca
8.88–9.02 mbsf
weighted mean
(4/4):
0.127±0.013 Ma
MSWD=0.59
127.50–127.52 mbsf
weighted mean
(12/12):
11.37±0.07 Ma
MSWD=1.65
564.92–564.93 mbsf
weighted mean
(16/16):
17.10±0.14 Ma
MSWD=0.71
640.13–640.16 mbsf
weighted mean
(17/17):
17.39±0.11 Ma
MSWD=1.39
709.14–709.16 mbsf
weighted mean
(6/10):
18.15±0.18 Ma
MSWD=0.95
709.17–709.19 mbsf
weighted mean
(5/10):
17.93±0.28 Ma
MSWD=0.83
831.66–831.68 mbsf
weighted mean
(15/15):
18.71±0.12 Ma
MSWD=0.93
953.28–953.31 mbsf
weighted mean
(15/15):
19.44±0.12 Ma
MSWD=1.06
953.54–953.56 mbsf
weighted mean
(12/12):
19.49±0.14 Ma
1093.00–1093.04 mbsf
weighted mean
(17/18):
20.01±0.12 Ma
MSWD=1.13
Age (Ma)

Fig. 2

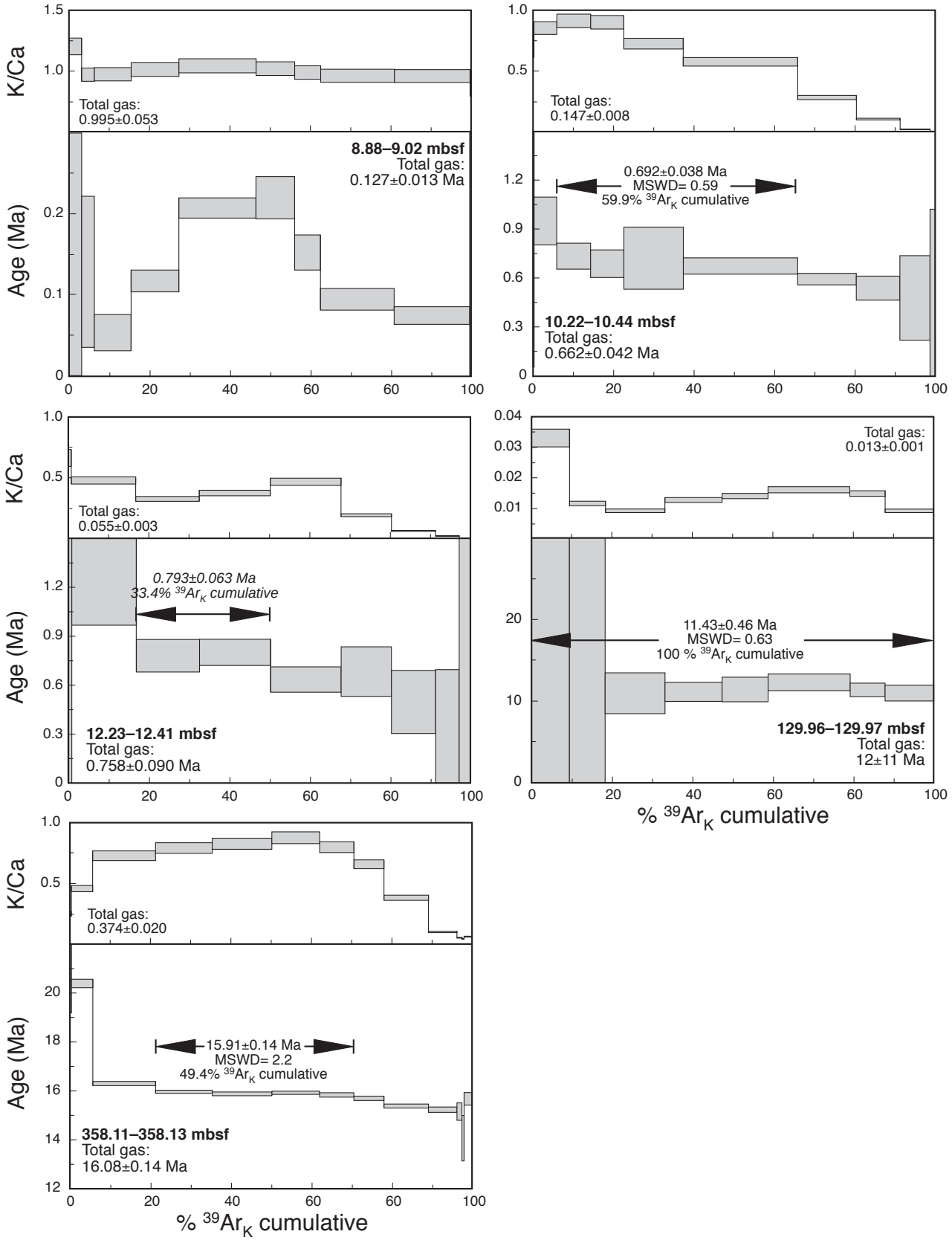
K/Ca
Age (Ma)
Total gas:
0.995±0.053
8.88–9.02 mbsf
Total gas:
0.127±0.013 Ma
Total gas:
0.147±0.008
0.692±0.038 Ma
MSWD= 0.59
59.9% 39ArK cumulative
10.22–10.44 mbsf
Total gas:
0.662±0.042 Ma
Total gas:
0.055±0.003
0.793±0.063 Ma
33.4% 39ArK cumulative
12.23–12.41 mbsf
Total gas:
0.758±0.090 Ma
Total gas:
0.013±0.001
11.43±0.46 Ma
MSWD= 0.63
100 % 39ArK cumulative
129.96–129.97 mbsf
Total gas:
12±11 Ma
% 39ArK cumulative
Total gas:
0.374±0.020
15.91±0.14 Ma
MSWD= 2.2
49.4% 39ArK cumulative
358.11–358.13 mbsf
Total gas:
16.08±0.14 Ma
% 39ArK cumulative

Fig. 3

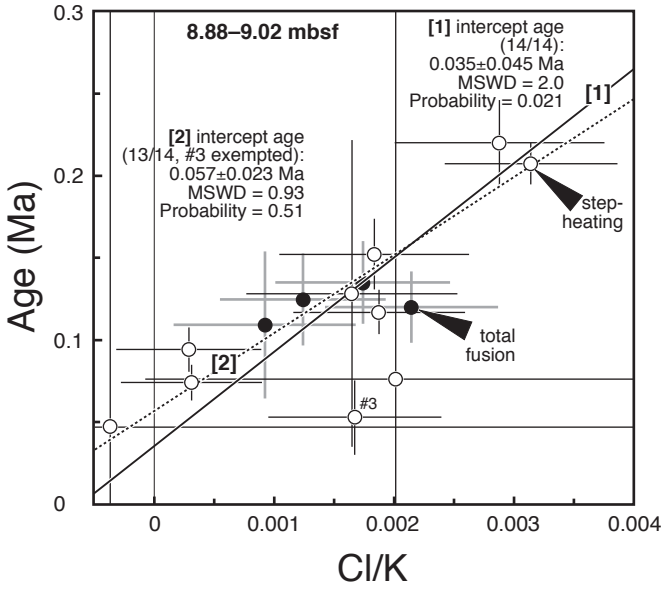
8.88–9.02 mbsf
[1] intercept age
(14/14):
0.035±0.045 Ma
MSWD = 2.0
Probability = 0.021
[1]
[2] intercept age
(13/14, #3 exempted):
0.057±0.023 Ma
MSWD = 0.93
Probability = 0.51
step-
heating
total
fusion
[2]
#3
Age (Ma)
Cl/K
0.3
0.2
0.1
0
0
0.001
0.002
0.003
0.004

Fig. 4

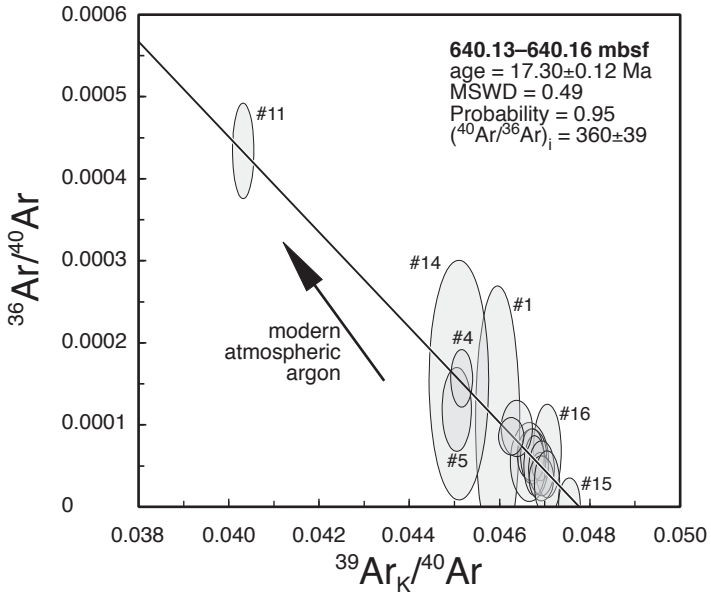
640.13–640.16 mbsf
age = 17.30±0.12 Ma
MSWD = 0.49
Probability = 0.95
(40Ar/36Ar)i = 360±39
#11
#14
#1
#4
#16
#5
#15
modern
atmospheric
argon
0.0006
0.0005
0.0004
0.0003
0.0002
0.0001
0
0.038
0.040
0.042
0.044
0.046
0.048
0.050
36Ar/40Ar
39ArK/40Ar

Fig. 5

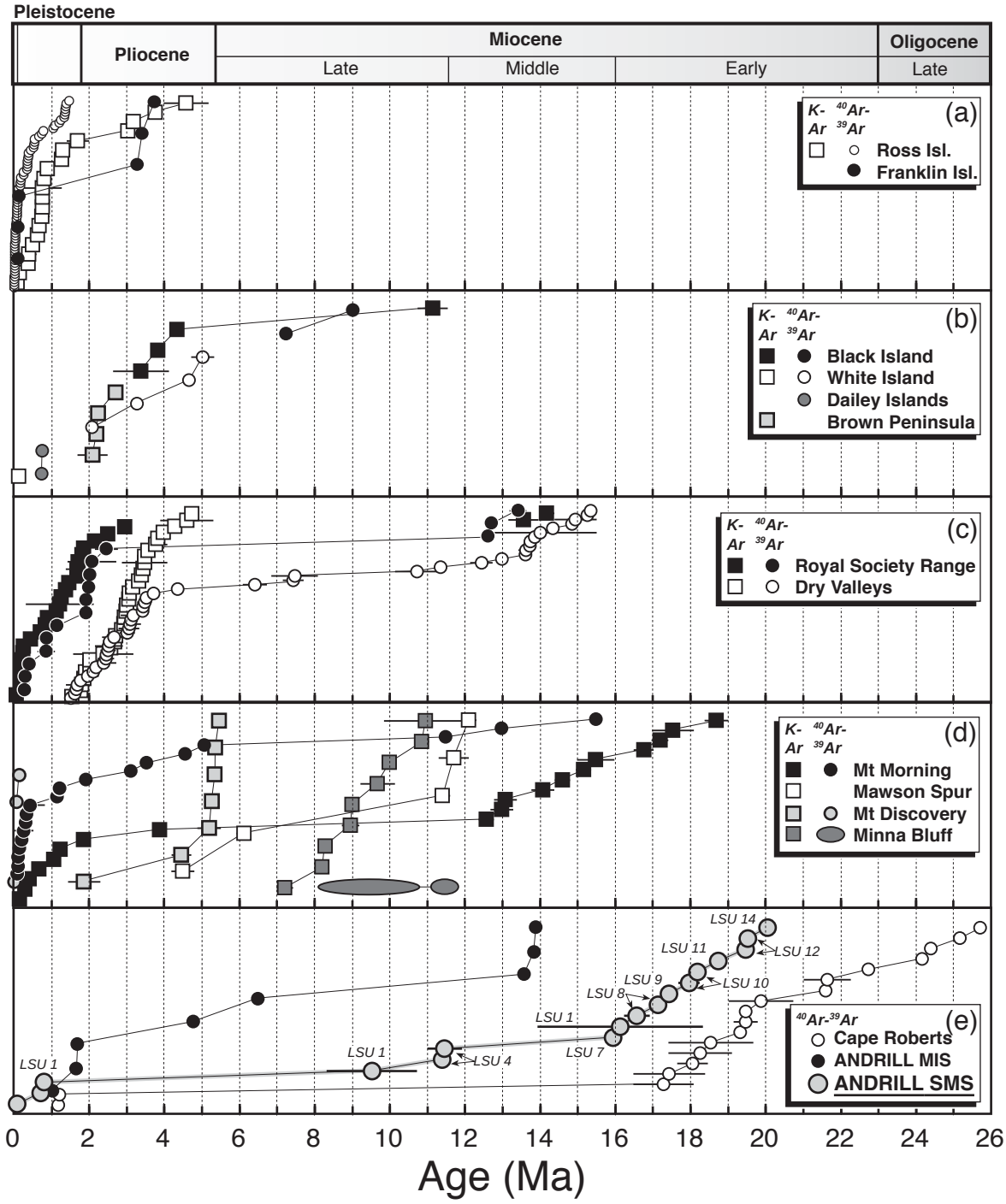
Pleistocene
Pliocene
Miocene
Late
Middle
Early
Oligocene
Late
K-Ar 40Ar-39Ar
(a)
Ross Isl.
Franklin Isl.
(b)
Black Island
White Island
Dailey Islands
Brown Peninsula
(c)
Royal Society Range
Dry Valleys
(d)
Mt Morning
Mawson Spur
Mt Discovery
Minna Bluff
(e)
40Ar-39Ar
Cape Roberts
ANDRILL MIS
ANDRILL SMS
LSU 1
LSU 1
LSU 4
LSU 1
LSU 7
LSU 8
LSU 9
LSU 10
LSU 11
LSU 12
LSU 14
0
2
4
6
8
10
12
14
16
18
20
22
24
26
Age (Ma)

Fig. 6

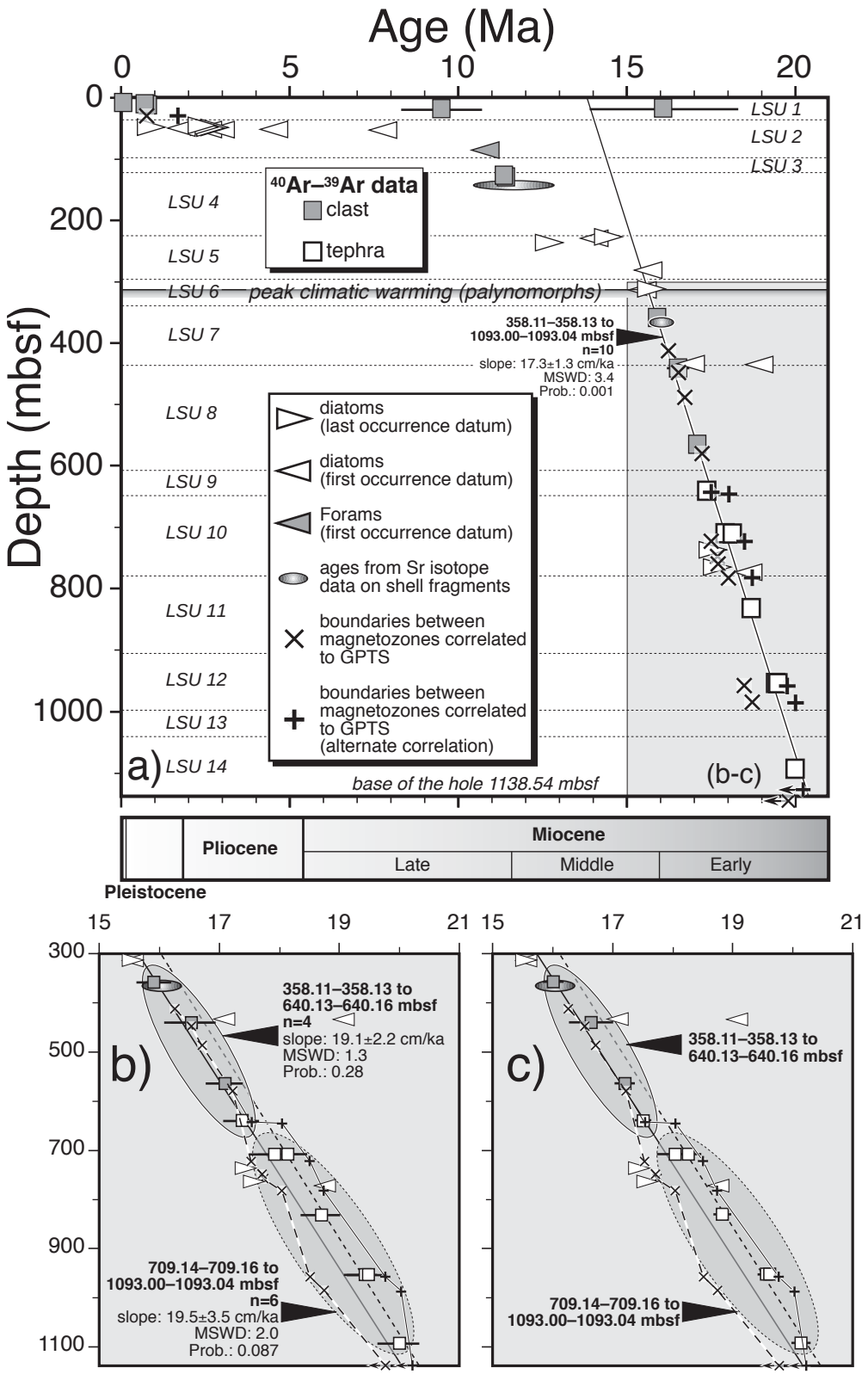
Age (Ma)
0
5
10
15
20
Depth (mbsf)
0
200
400
600
800
1000
LSU 1
LSU 2
LSU 3
LSU 4
LSU 5
LSU 6
LSU 7
LSU 8
LSU 9
LSU 10
LSU 11
LSU 12
LSU 13
LSU 14
peak climatic warming (palynomorphs)
40Ar–39Ar data
clast
tephra
358.11–358.13 to
1093.00–1093.04 mbsf
n=10
slope: 17.3±1.3 cm/ka
MSWD: 3.4
Prob.: 0.001
diatoms
(last occurrence datum)
diatoms
(first occurrence datum)
Forams
(first occurrence datum)
ages from Sr isotope
data on shell fragments
boundaries between
magnetozones correlated
to GPTS
boundaries between
magnetozones correlated
to GPTS
(alternate correlation)
a)
base of the hole 1138.54 mbsf
(b-c)
Pliocene
Miocene
Late
Middle
Early
Pleistocene
15
17
19
21
300
500
700
900
1100
b)
358.11–358.13 to
640.13–640.16 mbsf
n=4
slope: 19.1±2.2 cm/ka
MSWD: 1.3
Prob.: 0.28
709.14–709.16 to
1093.00–1093.04 mbsf
n=6
slope: 19.5±3.5 cm/ka
MSWD: 2.0
Prob.: 0.087
c)
358.11–358.13 to
640.13–640.16 mbsf
709.14–709.16 to
1093.00–1093.04 mbsf

Fig. 7

Electronic Supplementary Material

^{40}Ar–^{39}Ar dating of volcanogenic products from the AND-2A core (ANDRILL Southern McMurdo Sound Project, Antarctica): correlations with the Erebus Volcanic Province and implications for the age model of the core

by

G. Di Vincenzo, L. Bracciali, P. Del Carlo, K. Panter, S. Rocchi

1. Methods

Sample preparation and ^{40}Ar–^{39}Ar data collection were completed at IGG–CNR, Pisa (Italy). Samples selected for ^{40}Ar–^{39}Ar dating before processing, that is as received at IGG–CNR laboratory, are shown in Fig. S1. Samples affected by alteration, evident under the optical or electronic microscope, were rejected and not analyzed.

Polished thin sections from each sample were investigated by a light microscope and by scanning electron microscopy (SEM) using a Philips XL30 (using an accelerating voltage of 20 kV, sample current of 10 nA and 0.5 μm beam diameter) equipped with an energy dispersive system (EDS) at the Dipartimento di Scienze della Terra, Pisa.

After crushing and sieving, groundmasses and feldspars (plagioclase or alkali feldspar) were concentrated from different grain sizes (see Tables S1) using standard separation techniques, and further purified by hand-picking under a stereomicroscope. Groundmass separates were leached in an ultrasonic bath (heated to ~50°C) for 1 h in HCl 3.5 N and 1h in HNO_3 1N (Koppers et al. 2000). Feldspars were leached at room temperature in an ultrasonic bath for a few minutes. A longer leaching time (20 min) was used for alkali feldspar 8.88–9.02 mbsf, because of the presence of melt inclusions. After leaching, samples were washed in ultraclean water and dried on a hot plate at ~70°C. Splits of a few to several tens of milligrams of feldspars and groundmasses were wrapped in aluminium foil to form discs <9 mm in diameter and a few millimetres thick. Discs were stacked in pancake fashion within a quartz vial 9 mm in diameter. The stack was interspersed with splits of the standard Fish Canyon sanidine (FCs), every 4–6 mm to monitor the vertical neutron flux. *J* values for each stack position were monitored by analyzing 5 single crystals of FCs (assumed age 28.03 Ma, Jourdan and Renne 2007). Samples were irradiated in three distinct batches, for 5 h (PAV–64), 2 h (PAV–65) and 3 h (PAV–66), in the core of the TRIGA reactor at the University of Pavia (Italy). ^{40}Ar–^{39}Ar analyses were carried out using different laser extraction techniques and different laserprobes: (1) laser total fusion analysis of single or multi-grain splits of K-rich alkali feldspar using a CO_2 laser; (2) laser step-heating analysis using either a defocused Nd-doped yttrium-aluminium-garnet (Nd:YAG) laser (for groundmasses) or a defocused CO_2 laser (feldspars). After irradiation, splits consisting of one to a few grains of alkali feldspars (a few milligrams for total fusion analyses to a few tens of milligrams for step-heating analysis were used only for sample 8.88–9.02 mbsf) to a few tens of milligrams for plagioclase and groundmasses, were placed in 1.5- to 9-mm diameter holes (depending on the sample mass) of a copper holder and baked overnight. Total fusion analyses on alkali feldspars (including the fluence monitor FCs) were carried out using a continuous wave CO_2 laser defocused to 1 mm spot size. Step-heating analyses of groundmasses were performed using a continuous wave diode-pumped Nd:YAG laser, which was defocused to a 2 mm spot size and slowly rastered (at 0.1 mm s^{-1}) over the grains by a computer-controlled x–y stage to ensure even heating. One plagioclase and one alkali feldspar concentrates were incrementally heated using the CO_2 laser defocused to 3 mm spot size, which was manually rastered over the

grains to ensure even heating. Step-heating analyses were preceded by a total fusion analysis of mg-splits of the same separate in order to estimate a preliminary age then used to calculate the optimal sample weight for the step-heating run.

After cleanup (8–10 min, including 1 min of lasering for total fusion analyses and 15–20 min for step-heating experiments, including 8–9 min of lasering), using two Saes AP10 getters held at 400°C and one C–50 getter held at room temperature, extracted gases were equilibrated by automated valves into a MAP215–50 noble gas mass spectrometer fitted with a Balzers SEV217 secondary electron multiplier. Ar isotope peak intensities were measured ten times for a total of ~25 min. Blanks were analyzed every one to three analyses. Mass discrimination was monitored by analysis of air pipettes. At the time of data collection mean values were: 1.0051±0.0030 (±2SD, n=33) per atomic mass unit (AMU) for PAV–64, 1.0037±0.0016 (±2SD, n=13) AMU for PAV–65, and 1.0038±0.0018 (±2SD, n=22) AMU for PAV–66. Correction factors for interfering isotopes, determined on K- and Ca-rich glasses, were: $(^{40}Ar/^{39}Ar)_K$=0.0093, $(^{38}Ar/^{39}Ar)_K$=0.0129, $(^{39}Ar/^{37}Ar)_{Ca}$=0.00075 and $(^{36}Ar/^{37}Ar)_{Ca}$=0.00024. Data reduction was performed using the ArArCALC software (Koppers, 2002). Errors are given at 2σ and are quoted as: (1) analytical errors, including in-run statistics and uncertainties in the discrimination factor, interference corrections and procedural blanks; (2) internal errors, also including uncertainties in the *J* value; (3) full errors, also including uncertainties on the age of the flux monitor and those in the ^{40}K decay constants. Data corrected for post-irradiation decay, mass discrimination effects, isotopes derived from interference reactions and blanks are listed in Table S1. Ages listed in Table S1 were calculated using the IUGS recommended constants (Steiger and Jäger 1977). More details on the analytical procedures can be found in Di Vincenzo and Skála (2009). Error-weighted means and least squares fits were calculated using v. 3.00 of the Isoplot/Ex program (Ludwig 2003).

2. Features of dated rocks

Lithostratigraphic Unit 1 (0 – 37.01 mbsf)

Five samples, consisting of vesiculated lava clasts up to a few centimetres in size, were selected from the Lithostratigraphic Unit 1. A comprehensive description of these samples have been reported by Del Carlo et al. (2009) and will be only summarized here. Sample 8.88–9.02 (a fresh phonolite lava, Fig. S2a) is a lava clast that belongs to the first interval of the core recovered as loose samples in composite bags (bagged samples, i.e. the stratigraphic relationships are not recognizable). It is a fresh subangular glomeroporphyritic lava clast of phonolitic composition containing cm-sized anhedral anorthoclase (Fig. S3) phenocrysts with large glass inclusions (up to 0.5 mm), subhedral medium-grained phenocrysts of zoned clinopyroxene and minor olivine, set in an almost opaque glassy vesiculated groundmass. Flattened vesicles and elongated phenocrysts define a flowage texture.

Sample 10.22–10.44 is a variably vesiculated (5–20%) basanitic lava clast (Fig. S2b) characterized by a phenocrystic assemblage of euhedral skeletal olivine up to 4 mm in length and minor clinopyroxene in a brown glassy groundmass with microlites of clinopyroxene, plagioclase and oxides. Vesicles are irregular in shape and the groundmass consists of patches and streaks of a black to almost opaque glass (i.e., tachylite).

Sample 12.23–12.41 is a glomeroporphyritic vesiculated hawaiitic lava clast characterized by phenocrysts of zoned clinopyroxene (pale-green core to purple-brown rim) and minor olivine in a glassy groundmass that includes microlites of plagioclase, clinopyroxene and magnetite (Fig. S2c). The millimeter-sized rounded vesicles are partially filled with secondary calcite.

The hawaiitic lava clast 18.03–18.25 contains rounded vesicles and phenocrysts of zoned clinopyroxene and minor altered olivine in a glassy groundmass that includes microlites of clinopyroxene, plagioclase and oxides (Fig. S2d).

Sample 18.69–18.73 is a vesiculated (20%) lava clast with a subrounded shape. It is tephritic in composition and contains phenocrysts of clinopyroxene and minor bowlingitic olivine (Fig. S2e).

Lithostratigraphic Unit 4 (122.86 – 224.82 mbsf)

Samples 127.50–127.52 and 129.96–129.97 are two clasts from a diamictite, which is the main lithofacies of Lithostratigraphic Unit 4 (Fielding et al. 2008).

Sample 127.50–127.52 is 1 x 2 centimeter-sized subangular lava clast, consisting of a subaphyric trachyte (Fig. S2f) with scattered anorthoclase (Fig. S3) and green pyroxene microphenocrysts set in a trachytic-textured groundmass made of alkali feldspars and magnetite.

Sample 129.96–129.97 is a 1 x 3 centimeter-sized subangular porphyritic (15 vol%) basaltic lava clast with ~1 mm-sized phenocrysts of plagioclase, clinopyroxene and olivine pseudomorphs. The groundmass is made up of plagioclase microlites, altered glass and minor opaque minerals (Fig. S2g).

Lithostratigraphic Unit 7 (339.92 – 436.18 mbsf)

Sample 358.11–358.13 is a purplish to dark-brown, a few centimeters wide lava clast from a diamictite level. Euhedral magnetite phenocrysts and tiny plagioclase microphenocrysts, which define a pilotaxitic texture, are set in a holocrystalline groundmass with plagioclase, clinopyroxene, magnetite and apatite (Fig. S2h).

Lithostratigraphic Unit 8 (436.18 – 607.35)

Sample 440.83-440.86 is a 5 x 4 centimeter-sized, dark-brown to red, vesicular (15–20 vol%), poorly porphyritic (<1%), intermediate lava clast from a mudstone layer, with

microphenocrysts of plagioclase, abundant magnetite and alkali feldspar in a moderately altered holocrystalline groundmass (Fig. S2i).

Sample 564.92–564.93 is a grey, non-vesicular, porphyritic (10-15 vol%) felsic lava clast from a sandy conglomerate, with phenocrysts of alkali feldspar (~10 vol%), aegirinic clinopyroxene and minor magnetite set in a fine-grained holocrystalline groundmass. The groundmass contains plagioclase, alkali feldspar (mainly anorthoclase in composition, Fig. S3), clinopyroxene and magnetite.

Lithostratigraphic Unit 9 (607.35 – 648.74 mbsf)

Sample 640.13–640.16 belongs to a six-centimeter thick normally graded primary pyroclastic deposit within a sandstone interval and consists of grayish fine pumice lapilli to coarse ash. The pumice clasts are aphyric but in rare instances contain phenocrysts of alkali feldspar (mainly anorthoclase in composition, Fig. S3), the latter commonly found as isolated crystal fragments crystals up to ~0.5 mm in size (Fig. S2k). The pumice have very low alkali, magnesium and iron content pointing to a high degree of alteration (Panter et al., 2008). Pumice from the lapilli tuff are set in a fine-grained matrix of volcanic ash of the same chemical composition. Rare siliciclastic fragments (rounded quartz and lithic fragments) are also found. These observations, coupled with the gradational top and the loaded base of the layer, suggest that the deposit formed by direct sinking of a subaerial pyroclastic fallout (Panter et al., 2008).

Lithostratigraphic Unit 10 (648.74 – 778.34 mbsf)

Sample 709.14–709.16 and 709.17–709.19 are two similar ~3.5-cm thick layers made of rounded fine pumice lapilli, concentrated along ripple foresets. Pumice are subaphyric (with rare anorthoclase phenocrysts, Fig. S3) whose variably flattened vesicles are filled with calcite (Fig. S2l). Within the pumice clasts a significant amount of foreign detritus is present. Subangular to angular monomineralic clasts (up to ~0.3 mm in size) are represented by quartz, plagioclase, minor microcline and subordinate biotite and amphibole. The lithic component is dominated by volcanic clasts (orange-brownish, vesiculated sideromelane, minor tachylite and holocrystalline very fine-grained holocrystalline porphyritic lava). On the basis of lithological features, these deposits are interpreted as two pyroclastic fall events that settled through the water column to the seafloor and were then reworked by shallow water, wave-base processes.

Lithostratigraphic Unit 11 (778.34 – 904.66 mbsf)

Sample 831.66–831.68 represents the thickest (~1 cm thick) of three intervals in Lithostratigraphic Unit 11, where pumice clasts are concentrated. This clast-rich layer, in which the main component is represented by up to 4 mm-sized pumice, has gradational top and bottom contacts within a silty sandstone, which indicates a very weak reworking of a

pyroclastic fall deposit. Monomineralic fragments (alkali feldspar, plagioclase and minor quartz) along with lithic (mostly porphyritic volcanic) clasts also occur (Fig. S2m).

Lithostratigraphic Unit 12 (904.66 – 996.69 mbsf)

The analyzed samples from Lithostratigraphic Unit 12 represent two out of the six accumulations ranging from 2 to 10 cm thick (from the 953–964-mbsf interval) of yellow-grey pumices mixed with dark green highly angular clasts dispersed in a muddy fine-grained sandstone. The pumiceous layer of sample 953.28–953.31 (Fig. S2n) is made up of medium- to coarse-grained pumice fragments and also contains single crystals of euhedral anorthoclase (commonly broken) (Fig. S3), subordinate quartz and plagioclase as well as porphyritic pilotaxitic fragments (up to 1–2 mm sized). In sample 953.54–953.56, which is similar in overall composition to the former, pumices are concentrated in a ~1 cm-thick irregular strip and the amount of monomineralic sialic fragments is lower. Pumice are more altered with respect to those of the previous deposits, nevertheless the lack of foreign detritus in the matrix indicates that the pumice accumulations represent nearly primary tephra layers formed by pyroclastic activity.

Lithostratigraphic Unit 14 (1040.28 – 1138.54 mbsf)

The lowermost lithostragraphic unit consists of sandy diamictite and sandstone with dispersed clasts. Sample 1093.00–1093.04 was taken from a 6 cm-thick interval pumice-rich layer that shows sharp, highly angular to crenulated contacts with the surrounding sandstone. It is formed of dense non-vesicular glassy lense-shaped pumice clasts, subangular fresh monomineralic fragments [anorthoclase (Fig. S3), quartz and plagioclase] and felty to pilotaxitic textured volcanic clasts (Fig. S2o). The dark colour of the sample is due to the almost opaque matrix. Individual pumice are altered and replaced similarly to sample 953.54–953.56 and vary in colour from black to dark-green to brown. This layer is mostly matrix-supported, however, there are local areas where lense-shaped pumices are in contact and are imbricated. Foreign detritus is scarce. On the basis of the described features, this deposit represents a pyroclastic event that was very weakly reworked and later intruded by intra-formational sands (e.g., clastic dike-like).

References

Del Carlo P, Panter KS, Bassett K, Bracciali L, Di Vincenzo G, Rocchi S. (2009) Evidence for local volcanic sources in the upper lithostratigraphic unit of ANDRILL AND-2A core (Southern McMurdo Sound, Antarctica) and implications for paleoenvironment and subsidence in the western Victoria Land basin. Global Planet Change. doi: 10.1016/jgloplacha.2009.09.002

Di Vincenzo G, Skála R (2009) ^{40}Ar–^{39}Ar laser dating of tektites from the Cheb Basin (Czech republic): Evidence for coevality with moldavites and influence of the dating standard on the age of the Ries impact. Geochim Cosmochim Acta, 73:493–513

Fielding CR, Atkins CB, Bassett KN, Browne GH, Dunbar GB, Field BD, Frank TD, Panter KS, Pekar SF, Krissek LA, Passchier S (2008) Sedimentology and stratigraphy of the AND-2A core, ANDRILL Southern McMurdo Sound, Project, Antarctica. In: Harwood DM, Florindo F, Talarico F, Levy RH (eds), Studies from the ANDRILL, Southern McMurdo Sound Project, Antarctica. Terra Antarctica, 15 (in press)

Jourdan F, Renne PR (2007) Age calibration of the Fish Canyon sanidine $^{40}Ar/^{39}Ar$ dating standard using primary K–Ar standard. Geochim Cosmochim Acta 71:387–402

Koppers AAP (2002) ArArCALC—software for $^{40}Ar/^{39}Ar$ age calculations. Comp Geosci 28:605–619

Koppers AAP, Staudigel H, Wijbrans JR (2000) Dating crystalline groundmass separates of altered Cretaceous seamount basalts by the $^{40}Ar/^{39}Ar$ incremental heating technique. Chem Geol 166:139–158

Ludwig KR (2003) User's manual for Isoplot 3.00, a geochronological toolkit for Microsoft Excel. Berkeley Geochronology Center Spec Pub, 4:54 pp

Panter KS, Talarico F, Bassett K, Del Carlo P, Field B, Frank T, Hoffman S, Kuhn G, Reichelt L, Sandroni S, Tavini M, Bracciali L, Cornamusini G, von Eynatten H, Rocchi R (2008) Petrologic and Geochemical Composition of the AND-2A Core, ANDRILL Southern McMurdo Sound Project, Antarctica. In: Harwood DM, Florindo F, Talarico F, Levy RH (eds), Studies from the ANDRILL, Southern McMurdo Sound Project, Antarctica. Terra Antarctica, 15 (in press)

Steiger RH, Jäger E (1977) Subcommission on Geochronology: convention on the use of decay constants in geo- and cosmochronology. Earth Planet Sci Lett 36:359–362

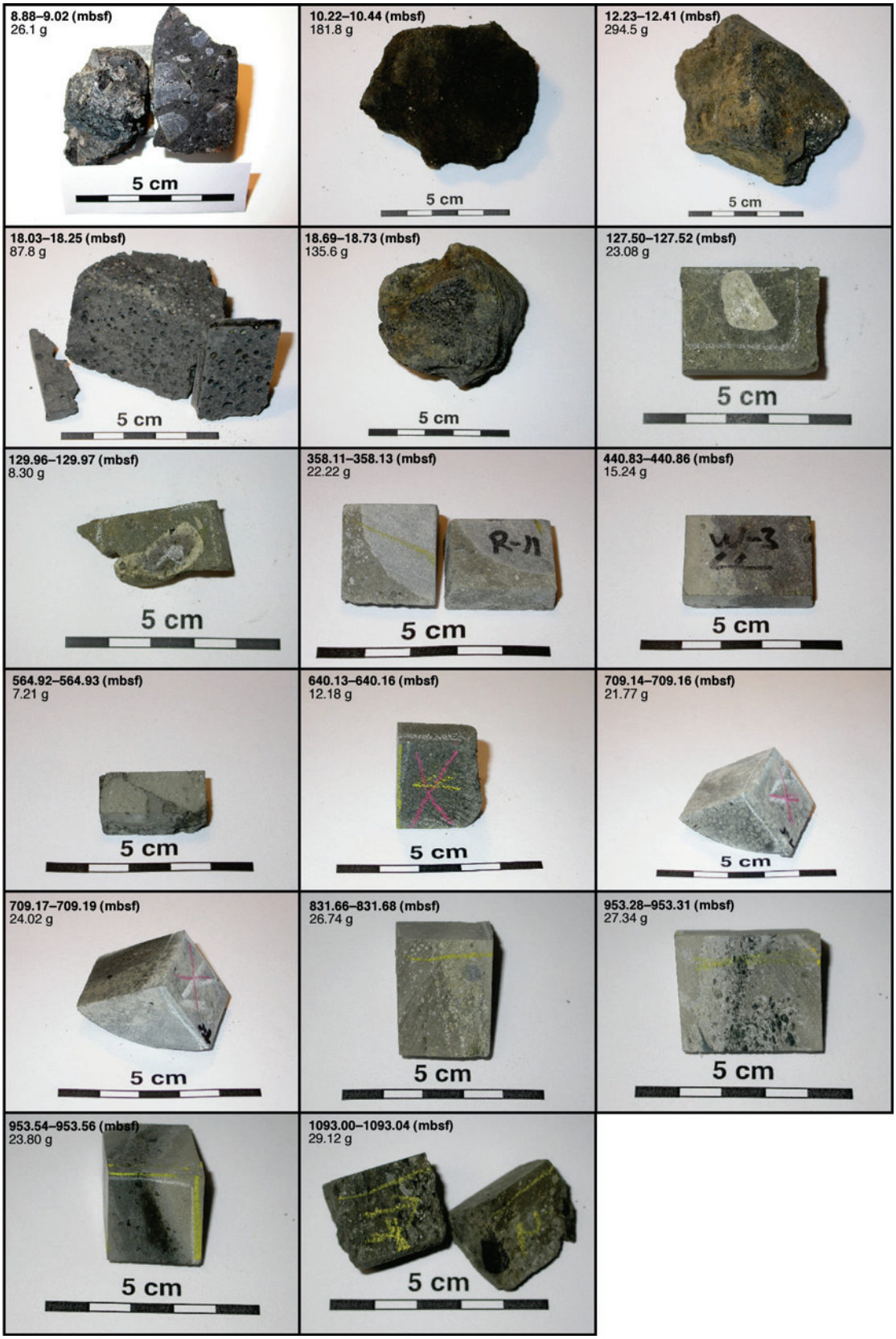

Fig. S1 Photographs showing samples selected for ^{40}Ar–^{39}Ar dating before processing.

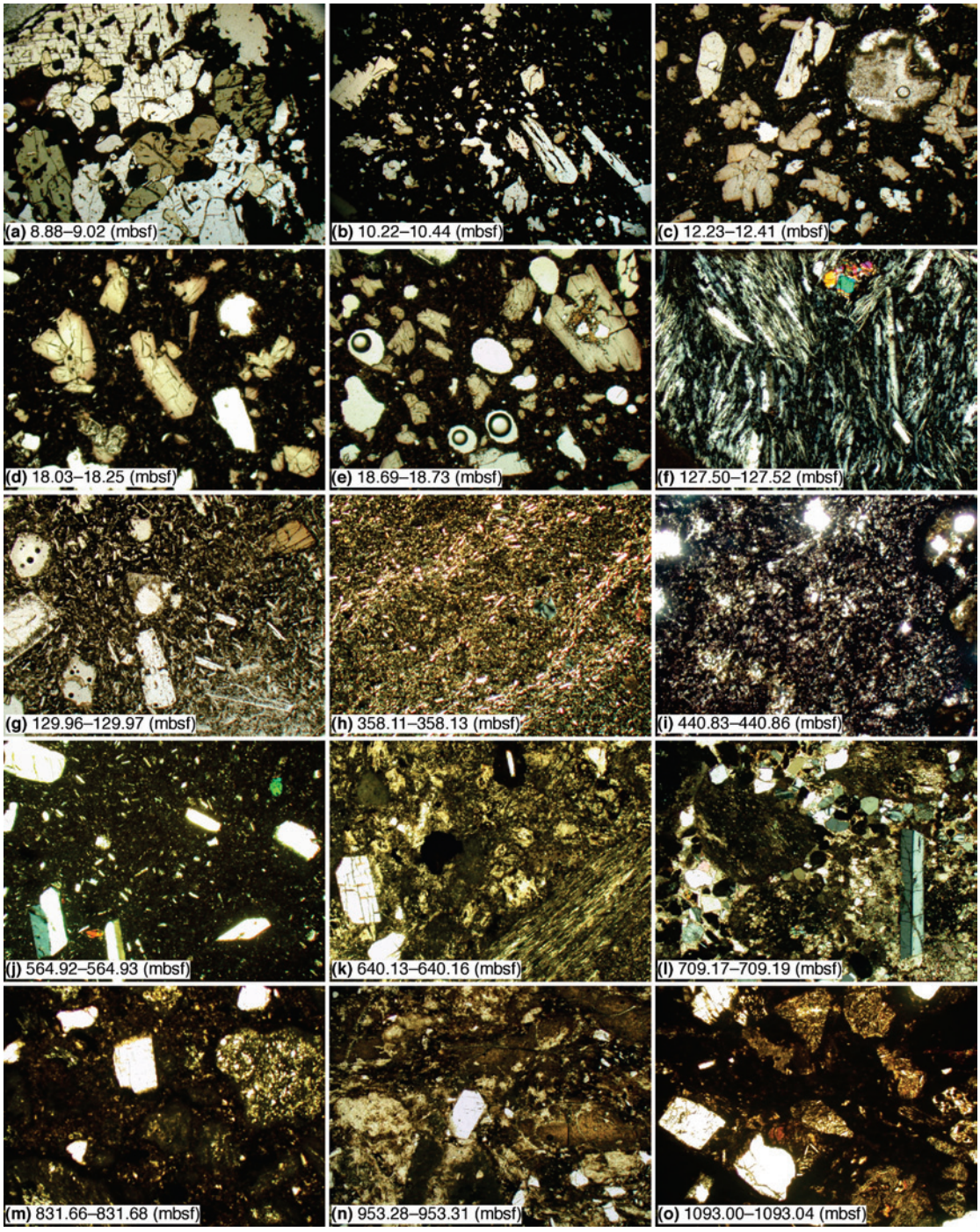

Fig. S2 Microphotographs showing the main petrographical features of samples selected for ^{40}Ar–^{39}Ar dating from the AND-2A core. **a** sample 8.88–9.02, phonolite lava clast with phenocrysts of coarse-grained alkali feldspar, medium-grained pale-green clinopyroxene and minor yellowish olivine set in an almost opaque groundmass, plane polarized light (PPL), field of view 5.5 mm. **b** sample 10.22–10.44, basanite lava clast with a phenocrystic assemblage of euhedral skeletal olivine and minor pale-brown clinopyroxene in a dark brown glassy groundmass, PPL, field of view 6 mm. **c** sample 12.23–12.41, hawaiite lava clast with glomeroporphyritic clusters of zoned (pale-green core to purple brown rim) clinopyroxene and minor olivine; the rounded vesicle (top-right of image) is partially filled with secondary calcite; PPL, field of view 3 mm. **d** sample 18.03–18.25, hawaiite lava clast with phenocrysts of zoned clinopyroxene and minor altered olivine in a glassy groundmass, PPL, field of view 3 mm. **e** sample 18.69–18.73, vesiculated tephrite lava clastcontaining phenocrysts of clinopyroxene and minor bowlingitic olivine; note the piroxene with a glassy core (top-right corner of image), PPL, field of view 5 mm. **f** sample 127.50–127.52, trachyte lava clast, with scattered alkali feldspar and minor green pyroxene (top-center) microphenocrysts set in a trachytic-textured groundmass made of alkali feldspars and magnetite, crossed polarized light (CPL), field of view 2 mm. **g** sample 129.96–129.97, basaltic lava clast with phenocrysts of plagioclase, clinopyroxene (top-right) and olivine pseudomorphs (center of

image), PPL, field of view 4 mm. **h** sample 358.11–358.13, euhedral magnetite phenocrysts and tiny plagioclase microphenocrysts define a pilotaxitic alignment in this basaltic lava clast, CPL, field of view 5.5 mm. **i** sample 440.83–440.86, vesicular poorly porphyritic intermediate lava clast with microphenocrysts of plagioclase, abundant magnetite and minor alkali feldspar in a moderately altered holocrystalline groundmass, PPL, field of view 3 mm. **j** sample 564.92–564.93, felsic lava clast with euhedral phenocrysts of alkali feldspar, aegirinic clinopyroxene and minor magnetite, CPL, field of view 5.5 mm. **k** sample 640.13–640.16, pyroclastic deposit containing angular vesiculated pumices (bottom-right of image), rarely with phenocrysts of alkali feldspar, the latter commonly found as isolated crystal fragments crystals (left of image), PPL, field of view 3 mm. **l** sample 709.17–709.19, coarse-grained pumiceous sandstone with a carbonatic cement found within a pumice- rich layer, note the three subaphyric pumices and the alkali feldspar (right), CPL, field of view 3 mm. **m** sample 831.66–831.68, pumice- rich layer with subordinate monomineralic feldspars grains, PPL, field of view 3 mm. **n** sample 953.28–953.31, pumiceous layer containing monomineralic euhedral alkali feldspar grains (e.g. center of image), PPL, field of view 3 mm. **o** sample 1093.00–1093.04, blocky dense clast, dark due to the almost opaque matrix, with strongly altered pumices, subangular fresh monomineralic felspars and quartz fragments and felty to pylotaxitic textured volcanic clasts, PPL, field of view 6 mm.

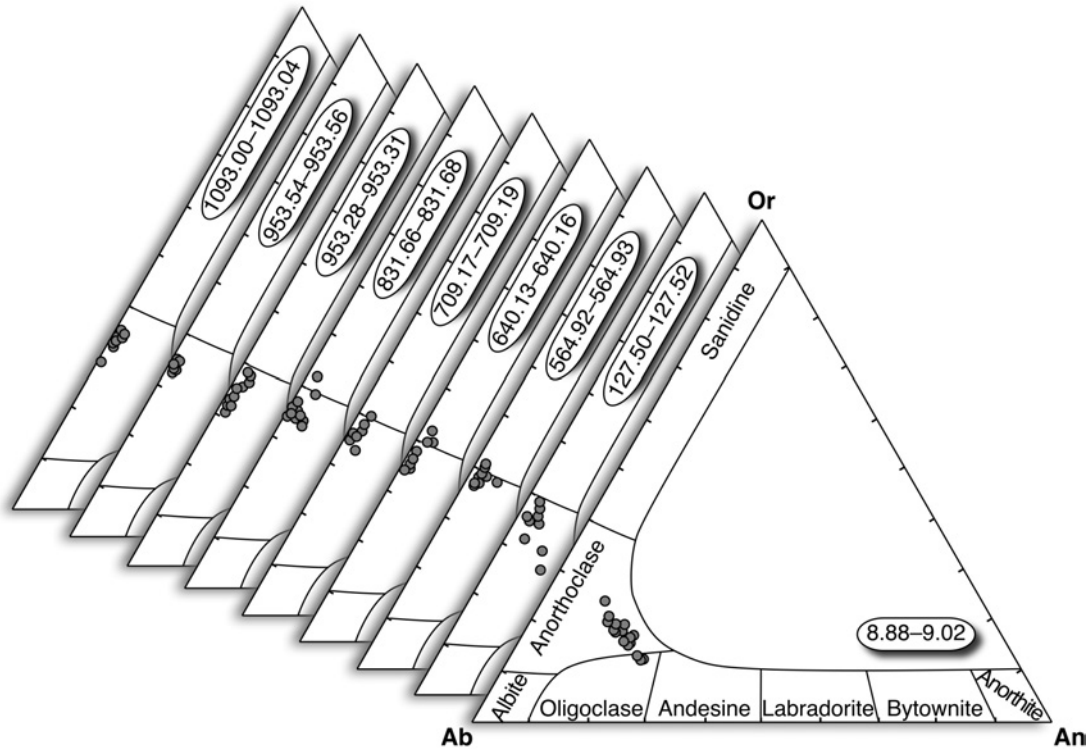

Fig. S3 K-feldspar–Albite–Anorthite triangular plot showing the compositions of alkali feldspars analyzed by the ^{40}Ar–^{39}Ar method.

Table S1 ^{40}Ar–^{39}Ar data of groundmasses and feldspars from volcanic samples of the AND-2A Core (ANDRILL SMS Project). Argon isotope concentrations are $x10^{-15}$ moles.

No.	weight (mg) laser power (W) # grains	$^{36}Ar_{(atm)}$	$^{37}Ar_{(Ca)}$	$^{38}Ar_{(Cl)}$	$^{39}Ar_{(K)}$	$^{40}Ar_{(Tot)}$	Age (Ma)	±2σ	$^{40}Ar^*$ %	$^{39}Ar_K$ %	Ca/K	±2σ
sample 8.88–9.02, anorthoclase grain size 0.30–0.50 mm, irradiation PAV–65, J=0.0001874±0.0000010												
Total fusion data data												
*1	3.5 mg	0.01440	1.000	0.00301	1.769	4.827	0.109	0.045	11.8	6.4	1.067	0.060
*2	8.2 mg	0.05453	3.382	0.01481	6.492	18.51	0.125	0.028	12.9	23.7	0.983	0.055
*3	7.0 mg	0.03000	2.543	0.01881	4.771	10.56	0.120	0.022	16.0	17.4	1.006	0.056
*4	8.3 mg	0.09283	3.278	0.01990	6.222	29.91	0.135	0.025	8.3	22.7	0.994	0.056
Total gas age							0.125	0.014				
Error-weighted mean age (4 of 4 steps), MSWD=0.59							0.124	0.014				
isochron age ($^{36}Ar/^{40}Ar$ vs. $^{39}Ar/^{40}Ar$ diagram), MSWD=0.89							0.107	0.039				
$^{40}Ar/^{36}Ar$ intercept							301	11				
sample 8.88–9.02, anorthoclase grain size 0.30–0.50 mm, 56.3 mg, irradiation PAV–65, J=0.0001874±0.0000010												
step-heating data												
1	0.3 W	0.32478	0.609	0.00511	1.382	96.28	0.08	0.35	0.3	3.1	0.832	0.048
2	0.5 W	0.02805	0.782	0.00433	1.428	8.831	0.128	0.094	6.1	3.2	1.033	0.059
3	0.8 W	0.02927	2.243	0.01265	4.113	9.293	0.053	0.022	6.9	9.2	1.029	0.058
4	1.3 W	0.02183	2.799	0.01840	5.337	8.298	0.117	0.014	22.1	11.9	0.990	0.056
5	2.0 W	0.04597	4.388	0.04982	8.624	18.87	0.207	0.013	27.9	19.2	0.960	0.054
6	2.8 W	0.02128	2.243	0.02283	4.313	9.095	0.220	0.026	30.7	9.6	0.981	0.055
7	4.1 W	0.00568	1.554	0.00975	2.893	2.979	0.152	0.022	43.3	6.4	1.013	0.058
8	6.6 W	0.00527	4.550	0.00435	8.244	3.857	0.094	0.013	58.4	18.4	1.041	0.058
9	8.0 W	0.01081	4.685	0.00482	8.460	5.047	0.074	0.011	36.2	18.8	1.045	0.058
10	10 W	0.00557	0.05867	bdl	0.09904	1.661	0.05	0.65	0.8	0.2	1.12	0.13
Total gas age							0.127	0.013				
Error-weighted mean age, no plateau							–	–				
sample 10.22–10.44, groundmass, grain size 0.30–0.50 mm, 50.4 mg, irradiation PAV–64, J=0.0004490±0.0000040												
step-heating data												
1	0.20 W	0.01617	0.1139	0.04020	0.1515	5.318	2.9	2.8	10.1	0.2	1.42	0.18
2	0.50 W	0.02453	2.167	0.8095	3.489	11.34	0.95	0.15	36.0	5.6	1.172	0.071
*3	0.70 W	0.01130	3.031	1.132	5.214	8.069	0.735	0.080	58.3	8.4	1.097	0.067
*4	0.90 W	0.01139	3.011	1.058	5.116	7.716	0.689	0.085	56.0	8.3	1.110	0.068
*5	1.2 W	0.4278	6.665	1.772	9.128	134.5	0.72	0.19	6.0	14.8	1.378	0.083
*6	1.5 W	0.1180	16.16	3.238	17.60	49.51	0.674	0.050	29.5	28.4	1.73	0.10
7	1.8 W	0.01514	16.74	1.579	9.013	11.08	0.594	0.035	59.2	14.6	3.50	0.21
8	2.5 W	0.01662	32.72	1.165	6.725	9.387	0.539	0.073	47.4	10.9	9.18	0.56
9	5.5 W	0.02198	96.49	0.7726	4.626	9.229	0.48	0.26	29.5	7.5	39.4	2.4
10	15 W	0.00925	45.40	0.1383	0.8167	2.990	0.25	0.77	8.5	1.3	104.9	6.5
Total gas age							0.662	0.042				
Error-weighted mean age (4 out of 10 steps), MSWD=0.59							0.692	0.038		59.9		
isochron age ($^{36}Ar/^{40}Ar$ vs. $^{39}Ar/^{40}Ar$ diagram), MSWD=0.89							0.691	0.047				
$^{40}Ar/^{36}Ar$ intercept							295.7	5.5				
sample 12.23–12.41, groundmass, grain size 0.30–0.50 mm, 52.1 mg, irradiation PAV–64, J=0.0004524±0.0000039												
step-heating data												
1	0.20 W	0.03455	0.1329	0.04024	0.1656	10.50	1.4	2.7	2.8	0.8	1.51	0.16
2	0.50 W	0.1205	3.773	0.5334	3.390	40.88	1.27	0.30	12.9	16.0	2.10	0.13
*3	0.70 W	0.03368	5.422	0.4906	3.328	13.13	0.78	0.10	24.2	15.7	3.07	0.19

Table S1 Continued

No.	# grains weight (mg) laser power (W)	$^{36}Ar_{(atm)}$	$^{37}Ar_{(Ca)}$	$^{38}Ar_{(Cl)}$	$^{39}Ar_{(K)}$	$^{40}Ar_{(Tot)}$	Age (Ma)	±2σ	$^{40}Ar^{*}$ %	$^{39}Ar_{K}$ %	Ca/K	±2σ
*4	0.90 W	0.02401	5.292	0.5356	3.729	10.76	0.801	0.080	33.9	17.6	2.68	0.16
5	1.2 W	0.03069	4.229	0.5670	3.714	11.96	0.634	0.078	24.1	17.6	2.15	0.14
6	1.5 W	0.03297	7.308	0.4157	2.643	11.95	0.68	0.15	18.5	12.5	5.22	0.32
7	1.8 W	0.02577	19.31	0.3731	2.319	9.026	0.50	0.19	15.6	11.0	15.7	1.0
8	2.5 W	0.01595	30.39	0.2187	1.249	5.219	0.33	0.37	9.6	5.9	45.9	2.8
9	5.0 W	0.01256	58.68	0.07965	0.4316	3.834	0.2	1.7	3.2	2.0	257	17
10	15 W	0.01204	69.03	0.02714	0.1709	3.649	0.4	5.7	2.5	0.8	762	69
Total gas age							0.758	0.090				
Error-weighted mean age, no plateau							*0.793*	*0.062*		*33.4*		
sample 18.03–18.25, groundmass, grain size 0.30–0.50 mm, 1.6 mg, irradiation PAV–64, J=0.0004551±0.0000032												
Total fusion data												
1	15 W	0.4074	9.471	0.1034	0.6397	133.2	16.1	2.2	9.6	–	27.9	1.8
sample 18.69–18.73, groundmass, grain size 0.30–0.50 mm, 2.5 mg, irradiation PAV–64, J=0.0004579±0.0000028												
Total fusion data												
1	15 W	0.5748	8.960	0.3159	1.655	189.2	9.5	1.2	10.2	–	10.21	0.64
sample 127.50–127.52, alkali feldspar, grain size >0.25 mm, irradiation PAV–64, J=0.0004590±0.0000028												
Total fusion data												
*1	1	0.00688	0.04639	bdl	1.952	28.76	11.30	0.15	92.9	3.8	0.0448	0.0070
*2	1	0.02792	0.50067	0.00272	9.131	133.7	11.345	0.049	93.8	17.7	0.1035	0.0058
*3	1	0.00353	0.13080	0.00026	5.087	71.10	11.368	0.069	98.5	9.9	0.0485	0.0030
*4	2	0.00240	0.09199	0.00044	4.365	60.91	11.385	0.071	98.8	8.5	0.0398	0.0028
*5	3	0.00333	0.13593	bdl	3.567	49.99	11.341	0.080	98.0	6.9	0.0719	0.0049
*6	5	0.00463	0.08861	0.00033	2.731	38.70	11.284	0.096	96.4	5.3	0.0612	0.0040
*7	1	0.01299	0.15140	bdl	5.419	78.34	11.350	0.069	95.0	10.5	0.0527	0.0032
*8	1	0.02048	0.11028	0.00022	3.807	58.32	11.334	0.096	89.6	7.4	0.0547	0.0039
9	3	0.03539	0.11703	0.00042	3.217	55.38	11.53	0.11	81.1	6.3	0.0686	0.0047
*10	7	0.00140	0.03789	bdl	1.313	18.50	11.37	0.19	97.7	2.6	0.0544	0.0078
*11	5	0.00328	0.02601	0.00069	0.9377	13.78	11.27	0.26	92.9	1.8	0.052	0.010
*12	1	0.01629	0.23925	0.00416	9.924	142.0	11.414	0.048	96.5	19.3	0.0455	0.0034
Total gas age							11.369	0.072				
Error-weighted mean age (11 of 12 runs), MSWD=1.65							11.363	0.072				
isochron age ($^{36}Ar/^{40}Ar$ vs. $^{39}Ar/^{40}Ar$ diagram), MSWD=1.48							11.347	0.080				
$^{40}Ar/^{36}Ar$ intercept							307	16				
sample 129.96–129.97, plagioclase, grain size 0.30–0.50 mm, 34.0 mg, irradiation PAV–64, J=0.0004597±0.0000028												
step-heating data												
*1	0.3 W	14.48	6.168	0.05097	0.3838	4285	10	115	0.1	9.4	30.3	2.7
*2	0.5 W	2.171	16.62	0.01193	0.3622	648.5	16	18	1.1	8.9	86.6	5.4
*3	0.8 W	0.4166	34.79	0.03193	0.6014	131.1	11.0	2.5	6.1	14.8	109.2	6.9
*4	1.3 W	0.04836	24.14	0.00715	0.5783	22.07	11.1	1.2	35.2	14.2	78.8	4.9
*5	2.0 W	0.04464	17.58	0.00511	0.4645	19.61	11.4	1.5	32.7	11.4	71.4	4.5
*6	3.3 W	0.12520	27.29	0.00602	0.8263	49.30	12.3	1.0	24.9	20.3	62.3	3.9
*7	4.3 W	0.01032	12.77	0.00198	0.3562	7.953	11.38	0.81	61.6	8.8	67.6	4.2
*8	10 W	0.01470	28.46	0.00150	0.4904	10.86	10.98	0.98	60.0	12.1	109.5	6.9
Total gas age							12	11				
Error-weighted mean age (8 of 8 steps), MSWD=0.63							11.43	0.46		100.0		

Table S1 Continued

No.	# grains weight (mg) laser power (W)	$^{36}Ar_{(atm)}$	$^{37}Ar_{(Ca)}$	$^{38}Ar_{(Cl)}$	$^{39}Ar_{(K)}$	$^{40}Ar_{(Tot)}$	Age (Ma)	±2σ	$^{40}Ar^{*}$ %	$^{39}Ar_{K}$ %	Ca/K	±2σ
isochron age ($^{36}Ar/^{40}Ar$ vs. $^{39}Ar/^{40}Ar$ diagram), MSWD=0.71							11.39	0.49				
$^{40}Ar/^{36}Ar$ intercept							296.0	2.3				
sample 358.11–358.13, groundmass, grain size 0.30–0.50 mm, 26.0 mg, irradiation PAV–66, J=0.0002761±0.0000011												
step-heating data												
1	0.15 W	0.0425	0.1996	0.00285	0.09441	16.68	21.7	2.5	24.8	0.3	3.99	0.29
2	0.30 W	0.0832	1.864	0.00583	1.610	90.89	20.40	0.18	72.9	5.3	2.19	0.12
3	0.45 W	0.0564	3.460	0.00064	4.745	172.6	16.299	0.089	90.3	15.6	1.376	0.076
*4	0.55 W	0.0247	2.882	0.00050	4.295	145.6	15.965	0.065	95.0	14.1	1.266	0.069
*5	0.70 W	0.0172	2.895	0.00147	4.508	149.4	15.877	0.081	96.6	14.8	1.212	0.066
*6	0.85 W	0.0139	2.193	0.00214	3.617	120.2	15.921	0.062	96.5	11.9	1.144	0.063
*7	1.0 W	0.0122	1.721	0.00084	2.589	86.23	15.830	0.091	95.8	8.5	1.255	0.069
8	1.2 W	0.0158	1.838	0.00257	2.277	76.71	15.691	0.090	93.9	7.5	1.523	0.083
9	1.5 W	0.0283	4.671	0.00515	3.373	113.0	15.381	0.082	92.6	11.1	2.61	0.14
10	2.0 W	0.0187	11.05	0.00524	2.150	71.53	15.23	0.11	92.3	7.1	9.69	0.53
11	3.0 W	0.0046	3.550	0.00045	0.3717	12.73	15.15	0.36	89.2	1.2	18.02	0.99
12	6.0 W	0.0043	1.854	bdl	0.1635	5.915	14.06	0.93	78.3	0.5	21.4	1.3
13	15 W	0.0079	4.921	0.00270	0.6012	21.34	15.68	0.26	89.0	2.0	15.44	0.85
Total gas age							16.08	0.14				
Error-weighted mean age (4 out of 13 steps), MSWD=2.23							15.91	0.14		49.4		
isochron age ($^{36}Ar/^{40}Ar$ vs. $^{39}Ar/^{40}Ar$ diagram), MSWD=1.81							15.74	0.32				
$^{40}Ar/^{36}Ar$ intercept							373	130				
sample 440.83–440.86, feldspars, grain size >0.18 mm, irradiation PAV–66, J=0.0002762±0.0000011												
Total fusion data												
1	1	0.02868	bdl	0.00188	0.8441	935.8	478.1	2.4	99.1	40.3	–	
2	1	0.01993	0.00290	0.00009	0.6835	299.9	202.6	1.8	98.0	32.6	0.008	0.012
*3	1	0.00103	0.00283	0.00020	0.2565	8.701	16.23	0.77	96.5	12.2	0.021	0.034
*4	1	0.00115	0.01055	0.00026	0.2994	10.36	16.60	0.35	96.7	14.3	0.066	0.020
5	1	0.00991	0.04717	0.00008	0.01196	25.48	756	36	88.5	0.6	7.44	0.77
Total gas age							277.7	2.7				
Error-weighted mean age (2 out of 5 runs), MSWD=0.74							16.54	0.34				
sample 564.92–564.93, alkali feldspar, grain size >0.25 mm, irradiation PAV–66, J=0.0002764±0.0000022												
Total fusion data												
*1	1	0.00247	0.03379	0.00024	1.172	41.24	17.15	0.13	98.2	5.6	0.0544	0.0048
*2	1	0.00106	0.00073	0.00011	0.3329	11.81	17.14	0.28	97.3	1.6	0.004	0.018
*3	3	0.00435	0.03915	0.00008	2.150	75.58	17.150	0.071	98.3	10.3	0.0344	0.0036
*4	1	0.00364	0.11080	bdl	1.815	63.64	17.104	0.113	98.3	8.7	0.1152	0.0080
*5	1	0.00252	0.04470	bdl	1.335	46.97	17.19	0.13	98.4	6.4	0.0632	0.0071
*6	1	0.00091	0.01017	bdl	0.6609	22.79	16.91	0.20	98.8	3.2	0.0290	0.0096
*7	3	0.00256	0.01238	0.00036	1.339	47.17	17.20	0.13	98.4	6.4	0.0174	0.0051
*8	3	0.00238	0.01133	bdl	1.021	35.76	17.04	0.14	98.0	4.9	0.0209	0.0062
*9	1	0.00368	0.01569	bdl	0.8246	29.48	17.09	0.14	96.3	3.9	0.0359	0.0065
*10	3	0.00371	0.01851	0.00058	1.438	50.53	17.056	0.098	97.8	6.9	0.0243	0.0049
*11	5	0.00424	0.03978	0.00036	1.776	62.61	17.145	0.092	98.0	8.5	0.0423	0.0044
*12	5	0.00348	0.02656	bdl	2.056	71.95	17.115	0.091	98.5	9.8	0.0244	0.0046
*13	1	0.00213	0.01325	bdl	0.5767	20.59	17.18	0.24	96.9	2.8	0.043	0.012
*14	3	0.00637	0.02152	bdl	1.445	51.64	17.089	0.095	96.3	6.9	0.0281	0.0043

Table S1 Continued

No.	# grains weight (mg) laser power (W)	$^{36}Ar_{(atm)}$	$^{37}Ar_{(Ca)}$	$^{38}Ar_{(Cl)}$	$^{39}Ar_{(K)}$	$^{40}Ar_{(Tot)}$	Age (Ma)	±2σ	$^{40}Ar^*$ %	$^{39}Ar_K$ %	Ca/K	±2σ
*15	3	0.00301	0.02043	0.00020	1.188	41.59	16.999	0.083	97.8	5.7	0.0324	0.0056
*16	3	0.00354	0.02802	bdl	1.789	62.50	17.054	0.085	98.3	8.5	0.0296	0.0034
Total gas age							17.11	0.14				
Error-weighted mean age (16 of 16 runs), MSWD=1.37							17.10	0.14				
isochron age ($^{36}Ar/^{40}Ar$ vs. $^{39}Ar/^{40}Ar$ diagram), MSWD=1.42							17.07	0.17				
$^{40}Ar/^{36}Ar$ intercept							324	86				
sample 640.13–640.16, alkali feldspar, grain size >0.18 mm, irradiation PAV–64, J=0.0004603±0.0000028												
Total fusion data												
*1	1	0.00079	0.00299	bdl	0.3403	7.408	17.42	0.72	96.8	1.4	0.017	0.035
*2	4	0.00099	0.00257	0.00075	1.448	30.78	17.40	0.19	99.0	6.0	0.0033	0.0041
*3	5	0.00225	0.01232	0.00017	1.611	34.48	17.35	0.16	98.0	6.7	0.0144	0.0057
*4	4	0.00506	0.02381	bdl	1.434	31.76	17.44	0.17	95.3	5.9	0.0313	0.0062
*5	5	0.00353	0.00259	0.00095	1.303	28.93	17.69	0.25	96.4	5.4	0.0038	0.0048
*6	5	0.00463	0.01176	bdl	2.389	51.67	17.40	0.13	97.3	9.9	0.0093	0.0030
*7	10	0.00374	0.04596	bdl	3.307	70.53	17.351	0.092	98.4	13.7	0.0262	0.0028
*8	5	0.00131	0.00462	0.00010	1.053	22.57	17.41	0.24	98.2	4.4	0.0083	0.0081
*9	7	0.00217	0.02690	0.00071	1.518	32.49	17.34	0.17	98.0	6.3	0.0334	0.0054
*10	5	0.00217	0.03239	0.00000	1.883	40.26	17.39	0.17	98.4	7.8	0.0325	0.0050
*11	5	0.01272	0.01328	0.00056	1.182	29.33	17.87	0.30	87.2	4.9	0.0212	0.0083
*12	5	0.00238	0.01157	0.00047	1.114	24.02	17.30	0.18	97.0	4.6	0.0196	0.0082
*13	5	0.00101	0.00823	0.00027	1.226	26.13	17.41	0.14	98.8	5.1	0.0127	0.0086
*14	1	0.00120	0.02422	0.00014	0.3461	7.676	17.48	0.67	95.3	1.4	0.132	0.041
*15	6	0.00030	0.01784	0.00074	1.607	33.81	17.34	0.14	99.7	6.7	0.021	0.010
*16	4	0.00150	0.01011	0.00008	0.9866	20.97	17.20	0.26	97.8	4.1	0.019	0.025
*17	7	0.00150	0.01610	bdl	1.385	29.52	17.35	0.16	98.5	5.7	0.022	0.011
Total gas age							17.41	0.11				
Error-weighted mean age (17 of 17 runs), MSWD=1.39							17.39	0.11				
isochron age ($^{36}Ar/^{40}Ar$ vs. $^{39}Ar/^{40}Ar$ diagram), MSWD=0.49							17.30	0.12				
$^{40}Ar/^{36}Ar$ intercept							360	40				
sample 709.14–709.16, alkali feldspar/plagiocalse, grain size >0.18 mm, irradiation PAV–64, J=0.0004614±0.0000028												
Total fusion data												
*1	1	0.03840	0.02621	0.00029	0.4404	21.03	18.21	0.77	46.0	11.8	0.112	0.027
*2	3	0.00232	0.01684	0.00002	1.0655	24.06	18.17	0.24	97.1	28.5	0.030	0.007
*3	3	0.00346	0.10423	0.00151	1.2331	27.91	18.06	0.21	96.3	33.0	0.159	0.012
4	3	0.00950	0.01957	0.00068	0.2263	19.74	61.2	1.7	85.8	6.1	0.163	0.041
5	3	0.00589	0.14108	0.00109	0.1172	4.699	20.9	2.0	63.0	3.1	2.27	0.15
6	3	0.02189	0.15972	0.00088	0.00707	8.645	239	42	25.2	0.2	42.6	5.9
*7	2	0.00442	0.02573	bdl	0.1848	5.517	18.9	1.0	76.3	4.9	0.263	0.063
*8	1	0.00002	0.00377	0.00071	0.1355	3.041	18.5	1.1	99.7	3.6	0.052	0.093
*9	2	0.00194	0.00183	0.00025	0.1204	3.306	18.8	1.2	82.6	3.2	0.029	0.084
10	2	0.00155	0.01106	0.00028	0.2047	5.387	19.93	0.79	91.5	5.5	0.102	0.061
Total gas age							21.47	0.25				
Error-weighted mean age (6 out of 10 runs), MSWD=0.95							18.15	0.18				
isochron age ($^{36}Ar/^{40}Ar$ vs. $^{39}Ar/^{40}Ar$ diagram), MSWD=1.09							18.13	0.20				
$^{40}Ar/^{36}Ar$ intercept							299	12				

Table S1 Continued

No.	# grains weight (mg) laser power (W)	$^{36}Ar_{(atm)}$	$^{37}Ar_{(Ca)}$	$^{38}Ar_{(Cl)}$	$^{39}Ar_{(K)}$	$^{40}Ar_{(Tot)}$	Age (Ma)	±2σ	$^{40}Ar^{*}$ %	$^{39}Ar_{K}$ %	Ca/K	±2σ
sample 709.17–709.19, alkali feldspar/plagioclase, grain size >0.18 mm, irradiation PAV–64, J=0.0004618±0.0000028												
Total fusion data												
*1	1	0.0102	0.0264	0.0004	0.9096	22.61	17.85	0.31	86.6	30.0	0.055	0.009
2	3	0.0060	0.0063	0.0003	0.4819	12.84	19.05	0.56	86.3	15.9	0.025	0.015
3	3	0.0106	0.0926	0.0007	0.4147	12.79	19.29	0.64	75.4	13.7	0.421	0.030
4	3	0.0012	bdl	bdl	0.2186	5.502	19.5	1.0	93.4	7.2	–	
5	4	0.0045	bdl	0.0005	0.0766	10.90	101.3	3.2	87.8	2.5	–	
6	4	0.0134	0.2022	0.0004	0.1640	13.60	48.4	1.6	71.0	5.4	2.33	0.15
*7	2	0.0040	0.0004	0.0004	0.1662	4.957	18.8	1.3	76.2	5.5	0.005	0.087
*8	2	0.0012	0.0032	0.0006	0.2395	5.548	17.99	0.80	93.6	7.9	0.025	0.054
*9	2	0.0012	0.0032	0.0002	0.2607	5.962	17.81	0.79	93.9	8.6	0.023	0.053
*10	2	0.0016	0.0006	bdl	0.09820	2.682	18.6	1.3	82.0	3.2	0.01	0.16
Total gas age							22.26	0.28				
Error-weighted mean age (5 out of 10 runs), MSWD=0.83							17.93	0.28				
isochron age ($^{36}Ar/^{40}Ar$ vs. $^{39}Ar/^{40}Ar$ diagram), MSWD=0.43							17.44	0.86				
$^{40}Ar/^{36}Ar$ intercept							351	92				
sample 831.66–831.68, alkali feldspar, grain size >0.25 mm, irradiation PAV–64, J=0.0004623±0.0000028												
Total fusion data												
*1	1	0.01925	0.00147	bdl	3.252	79.10	18.73	0.12	92.8	13.8	0.0009	0.0024
*2	1	0.00353	0.00523	0.00061	4.039	91.92	18.67	0.09	98.8	17.1	0.0024	0.0023
*3	1	0.00363	0.04793	bdl	1.993	46.04	18.72	0.14	97.6	8.4	0.0454	0.0053
*4	1	0.00303	0.00220	0.00088	1.285	29.75	18.64	0.21	97.0	5.4	0.0032	0.0077
*5	1	0.00232	0.02308	0.00053	1.203	27.98	18.83	0.22	97.5	5.1	0.0362	0.0085
*6	3	0.00246	0.02572	0.00121	1.610	36.80	18.59	0.20	98.0	6.8	0.0301	0.0062
*7	1	0.00456	0.00202	0.00047	1.426	33.33	18.62	0.17	95.9	6.0	0.003	0.011
*8	1	0.00195	bdl	bdl	1.062	24.66	18.82	0.23	97.6	4.5	–	
*9	1	0.00133	0.05870	bdl	1.175	26.89	18.71	0.22	98.5	5.0	0.0943	0.0119
*10	1	0.00131	bdl	0.00053	0.9832	22.57	18.72	0.25	98.2	4.2	–	
*11	1	0.00097	bdl	0.00161	0.8143	18.77	18.83	0.22	98.4	3.5	–	
*12	3	0.00177	0.00090	0.00091	1.668	38.22	18.75	0.15	98.6	7.1	0.0010	0.0144
*13	1	0.00089	0.00330	0.00029	0.4195	9.523	18.32	0.50	97.2	1.8	0.0148	0.0375
*14	3	0.00153	0.00310	0.00019	1.514	34.55	18.69	0.15	98.7	6.4	0.0039	0.0125
*15	3	0.00092	0.00026	0.00004	1.148	26.38	18.88	0.21	98.9	4.9	0.0004	0.0220
Total gas age							18.71	0.12				
Error-weighted mean age (15 of 15 runs), MSWD=0.93							18.71	0.12				
isochron age ($^{36}Ar/^{40}Ar$ vs. $^{39}Ar/^{40}Ar$ diagram), MSWD=0.98							18.69	0.13				
$^{40}Ar/^{36}Ar$ intercept							304	32				
sample 953.28–953.31, alkali feldspar, grain size >0.25 mm, irradiation PAV–64, J=0.0004629±0.0000028												
Total fusion data												
*1	1	0.01191	0.01684	0.00116	5.079	122.5	19.463	0.092	97.1	10.6	0.0063	0.0013
*2	1	0.02354	0.01757	0.00058	4.670	116.2	19.421	0.084	94.0	9.7	0.0071	0.0020
*3	1	0.00596	0.00630	bdl	2.588	62.16	19.39	0.13	97.1	5.4	0.0046	0.0048
*4	1	0.00596	0.05627	bdl	5.929	140.8	19.484	0.079	98.7	12.3	0.0179	0.0020
*5	1	0.00766	0.00982	0.00044	4.105	98.21	19.413	0.091	97.7	8.5	0.0045	0.0019
*6	1	0.00211	0.02411	0.00131	2.135	50.37	19.35	0.14	98.7	4.4	0.0213	0.0057
*7	1	0.00195	0.00975	bdl	2.454	57.92	19.41	0.15	99.0	5.1	0.0075	0.0051
*8	1	0.00200	0.03461	0.00066	2.022	48.02	19.48	0.15	98.7	4.2	0.0323	0.0064

Table S1 Continued

No.	# grains weight (mg) laser power (W)	$^{36}Ar_{(atm)}$	$^{37}Ar_{(Ca)}$	$^{38}Ar_{(Cl)}$	$^{39}Ar_{(K)}$	$^{40}Ar_{(Tot)}$	Age (Ma)	±2σ	$^{40}Ar^{*}$ %	$^{39}Ar_{K}$ %	Ca/K	±2σ
*9	1	0.00371	0.00672	bdl	2.201	52.91	19.56	0.13	97.9	4.6	0.0058	0.0054
*10	1	0.00237	0.00618	0.00111	2.482	59.01	19.51	0.15	98.8	5.2	0.0047	0.0050
*11	1	0.00271	bdl	bdl	2.027	48.07	19.37	0.12	98.3	4.2	–	
*12	5	0.00382	0.03530	bdl	4.360	103.1	19.43	0.10	98.9	9.1	0.0153	0.0028
*13	2	0.00255	0.02238	bdl	3.409	80.63	19.459	0.081	99.0	7.1	0.0124	0.0035
*14	1	0.00169	0.01094	bdl	2.139	50.80	19.53	0.14	99.0	4.5	0.0096	0.0119
*15	1	0.00247	0.02281	0.00052	2.453	57.85	19.34	0.12	98.7	5.1	0.0175	0.0087
Total gas age							19.44	0.12				
Error-weighted mean age (15 of 15 runs), MSWD=1.06							19.44	0.12				
isochron age ($^{36}Ar/^{40}Ar$ vs. $^{39}Ar/^{40}Ar$ diagram), MSWD=1.14							19.45	0.13				
$^{40}Ar/^{36}Ar$ intercept							292	28				
sample 953.54–953.56, alkali feldspar, grain size >0.25 mm, irradiation PAV–64, J=0.0004640±0.0000028												
Total fusion data												
*1	1	0.00865	0.00404	0.00006	0.7982	21.10	19.34	0.31	87.8	5.7	0.010	0.010
*2	1	0.00387	0.00402	bdl	0.8700	21.57	19.55	0.34	94.7	6.2	0.009	0.008
*3	1	0.00113	0.00238	0.00011	1.050	24.95	19.51	0.27	98.6	7.5	0.004	0.013
*4	1	0.01611	0.09551	0.00117	1.095	30.51	19.57	0.25	84.4	7.9	0.164	0.013
*5	2	0.00159	0.00190	0.00011	1.122	26.61	19.39	0.27	98.2	8.1	0.003	0.008
*6	3	0.00474	0.01119	0.00002	2.601	62.66	19.61	0.14	97.7	18.7	0.008	0.003
*7	1	0.00047	0.00007	0.00070	0.5905	14.13	19.73	0.39	99.0	4.2	0.000	0.023
*8	1	0.00242	0.00246	bdl	0.9783	23.62	19.49	0.22	96.9	7.0	0.005	0.016
*9	1	0.00069	0.00080	bdl	0.8507	20.07	19.44	0.21	98.9	6.1	0.002	0.013
*10	2	0.00631	0.00081	bdl	0.9551	24.00	19.30	0.27	92.2	6.9	0.002	0.011
*11	3	0.00431	0.00862	bdl	1.282	31.03	19.33	0.18	95.9	9.2	0.013	0.008
*12	6	0.00509	0.02140	0.00036	1.726	42.06	19.56	0.21	96.4	12.4	0.023	0.012
Total gas age							19.49	0.14				
Error-weighted mean age (12 of 12 runs), MSWD=1.11							19.49	0.14				
isochron age ($^{36}Ar/^{40}Ar$ vs. $^{39}Ar/^{40}Ar$ diagram), MSWD=1.21							19.50	0.15				
$^{40}Ar/^{36}Ar$ intercept							293	23				
sample 1093.00–1093.04, alkali feldspar, grain size >0.25 mm, irradiation PAV–64, J=0.0004645±0.0000028												
Total fusion data												
*1	1	0.00860	0.03536	0.00130	3.273	81.05	19.99	0.12	96.8	4.5	0.0204	0.0043
*2	1	0.03497	0.02248	0.00326	4.290	113.4	20.013	0.092	90.9	5.9	0.0099	0.0012
*3	1	0.04713	0.08456	bdl	5.061	135.3	19.978	0.099	89.7	6.9	0.0315	0.0022
*4	1	0.10761	0.01469	0.00261	2.209	84.89	20.03	0.26	62.5	3.0	0.0125	0.0040
*5	1	0.47887	0.01817	0.00262	3.170	217.8	20.06	0.57	35.0	4.3	0.0108	0.0027
*6	1	0.01003	0.07354	0.00086	3.036	76.26	20.12	0.12	96.1	4.2	0.0457	0.0038
*7	1	0.00489	0.04719	0.00074	3.065	75.19	20.05	0.10	98.0	4.2	0.0290	0.0025
*8	1	0.01018	0.14663	bdl	8.070	196.8	20.008	0.077	98.4	11.1	0.0343	0.0024
9	1	0.02552	0.07371	0.00239	5.054	127.4	19.758	0.093	94.0	6.9	0.0275	0.0023
*10	1	0.02030	0.03709	0.00027	7.233	179.7	20.013	0.091	96.6	9.9	0.0097	0.0016
*11	1	0.00581	0.01489	bdl	2.780	68.47	20.01	0.13	97.5	3.8	0.0101	0.0030
*12	1	0.02047	0.13845	0.00100	5.251	132.4	20.049	0.087	95.4	7.2	0.0497	0.0042
*13	1	0.07014	0.25224	0.00367	5.403	150.1	19.955	0.099	86.2	7.4	0.0881	0.0070
*14	1	0.01867	0.00398	0.00063	3.840	98.34	20.14	0.10	94.4	5.3	0.0020	0.0049
*15	1	0.00191	0.01517	0.00026	1.603	39.07	20.01	0.19	98.5	2.2	0.018	0.011
*16	1	0.00350	0.00540	bdl	2.171	52.86	19.89	0.16	98.0	3.0	0.0047	0.0077

Table S1 Continued

No.	# grains weight (mg) laser power (W)	$^{36}Ar_{(atm)}$	$^{37}Ar_{(Ca)}$	$^{38}Ar_{(Cl)}$	$^{39}Ar_{(K)}$	$^{40}Ar_{(Tot)}$	Age (Ma)	±2σ	$^{40}Ar^{*}$ %	$^{39}Ar_{K}$ %	Ca/K	±2σ
*17	6	0.01137	0.05664	bdl	5.413	132.9	19.938	0.083	97.4	7.4	0.0197	0.0039
*18	1	0.00286	0.00750	0.00046	1.956	47.88	20.04	0.12	98.2	2.7	0.007	0.016
Total gas age							20.00	0.13				
Error-weighted mean age (17 out of 18 runs), MSWD=1.13							20.01	0.12				
isochron age ($^{36}Ar/^{40}Ar$ vs. $^{39}Ar/^{40}Ar$ diagram), MSWD=1.20							20.01	0.13				
$^{40}Ar/^{36}Ar$ intercept							295.4	4.0				

Errors on the single runs are analytical uncertainties. Errors on total gas and error-weighted mean ages also include the unceratinty in *J* value. *, runs used in the weighted mean calculation. bdl, below detection limit